



Originally published as:

Hofmann, H., Zimmermann, G., Farkas, M. P., Huenges, E., Zang, A., Leonhardt, M., Kwiatek, G., Martinez Garzon, P., Bohnhoff, M., Min, K.-B., Fokker, P., Westaway, R., Bethmann, F., Meier, P., Yoon, K. S., Choi, J. W., Lee, T. J., Kim, K. Y. (2019): First field application of cyclic soft stimulation at the Pohang Enhanced Geothermal System site in Korea. - *Geophysical Journal International*, 217, 2, pp. 926—949.

DOI: <http://doi.org/10.1093/gji/ggz058>

First field application of cyclic soft stimulation at the Pohang Enhanced Geothermal System site in Korea

Hannes Hofmann¹,¹ Günter Zimmermann,^{1,2} Marton Farkas,¹ Ernst Huenges,^{1,2} Arno Zang,^{3,4} Maria Leonhardt,⁵ Grzegorz Kwiatek,⁵ Patricia Martinez-Garzon,⁵ Marco Bohnhoff,^{5,6} Ki-Bok Min,⁷ Peter Fokker,^{8,9} Rob Westaway,¹⁰ Falko Bethmann,¹¹ Peter Meier,¹¹ Kern Shin Yoon,¹² Jai Won Choi,¹² Tae Jong Lee¹³ and Kwang Yeom Kim¹⁴

¹Helmholtz Centre Potsdam GFZ German Research Centre for Geosciences, Section 4.8 Geoenergy, Telegrafenberg, 14473 Potsdam, Germany.

E-mail: hannes.hofmann@gfz-potsdam.de

²Technische Universität Berlin, Straße des 17. Juni 135, 10623 Berlin, Germany

³Helmholtz Centre Potsdam GFZ German Research Centre for Geosciences, Section 2.6 Seismic Hazard and Risk Dynamics, Telegrafenberg, 14473 Potsdam, Germany

⁴Universität Potsdam, Am Neuen Palais 10, 14469 Potsdam, Germany

⁵Helmholtz Centre Potsdam GFZ German Research Centre for Geosciences, Section 4.2 Geomechanics and Scientific Drilling, Telegrafenberg, 14473 Potsdam, Germany

⁶Freie Universität Berlin, Department of Earth Sciences, Malteser Straße 74–100, 12249 Berlin, Germany

⁷Seoul National University, Department of Energy Resources Engineering and Research Institute of Energy and Resources, 1 Gwanak-ro, Gwanak-gu, Seoul 08826, South Korea

⁸TNO Applied Geosciences, Princetonlaan 6, 3584 CB Utrecht, The Netherlands

⁹Utrecht University, Bestuursgebouw, Heidelberglaan 8, 3584 CS Utrecht, The Netherlands

¹⁰University of Glasgow, School of Engineering, James Watt (South) Building, Glasgow G128QQ, United Kingdom

¹¹Geo-Energie Suisse AG, Reitergasse 11, 8004 Zürich, Switzerland

¹²NexGeo Inc., 39 Yangjae-ro, Songpa-gu, Seoul 05703, South Korea

¹³Korea Institute of Geoscience and Mineral Resources, 124 Gwahak-ro, Yuseong-gu, Daejeon 34132, South Korea

¹⁴Korea Institute of Civil Engineering and Building Technology, 283 Goyangdae-ro, Ilsanseo-gu, Gyeonggi 10223, South Korea

Accepted 2019 January 29. Received 2019 January 23; in original form 2018 July 19

SUMMARY

Large-magnitude fluid-injection induced seismic events are a potential risk for geothermal energy developments worldwide. One potential risk mitigation measure is the application of cyclic injection schemes. After validation at small (laboratory) and meso (mine) scale, the concept has now been applied for the first time at field scale at the Pohang Enhanced Geothermal System (EGS) site in Korea.

From 7 August until 14 August 2017 a total of 1756 m³ of surface water was injected into Pohang well PX-1 at flow rates between 1 and 10 l s⁻¹, with a maximum wellhead pressure (WHP) of 22.8 MPa, according to a site-specific cyclic soft stimulation schedule and traffic light system. A total of 52 induced microearthquakes were detected in real-time during and shortly after the injection, the largest of M_w 1.9. After that event a total of 1771 m³ of water was produced back from the well over roughly 1 month, during which time no larger-magnitude seismic event was observed. The hydraulic data set exhibits pressure-dependent injectivity increase with fracture opening between 15 and 17 MPa WHP, but no significant permanent transmissivity increase was observed.

The maximum magnitude of the induced seismicity during the stimulation period was below the target threshold of M_w 2.0 and additional knowledge about the stimulated reservoir was gained. Additionally, the technical feasibility of cyclic injection at field scale was evaluated. The major factors that limited the maximum earthquake magnitude are believed to be: limiting the injected net fluid volume, flowback after the occurrence of the largest induced seismic event, using a cyclic injection scheme, the application of a traffic light system, and including *a priori* information from previous investigations and operations in the treatment design.

Key words: Cyclic soft stimulation (CSS); induced seismicity; risk mitigation; enhanced geothermal systems (EGS); granite; Pohang (Korea).

1 INTRODUCTION

Future geological energy technologies such as unconventional hydrocarbons and geothermal energy rely not only on production but also on safe injection of fluid into the subsurface. In deep geothermal energy applications two types of fluid injection are performed: First, to extract heat from the Earth and use it for heating or electricity generation, a hot and permeable geological formation is required from which a fluid (i.e. hot water or steam) can be produced. After heat extraction, this produced fluid is often re-injected into the reservoir for disposal and reservoir management (e.g. Stefansson 1997; Kaya *et al.* 2011). Second, in Enhanced Geothermal Systems (EGS), where initial reservoir permeability is too low or reservoir access is insufficient, fluid may also be injected for hydraulic stimulation treatments, to improve well performance by creating new flow paths or enhancing existing ones (e.g. McClure & Horne 2014; Schulte *et al.* 2010).

Fluid injection operations for well stimulation are known to induce seismic events, which are in most cases of low magnitude and thus too small to be felt or instrumentally detected at the surface (e.g. Majer *et al.* 2007). Information on seismic events is vital in order to map and understand the natural or engineered geothermal reservoir and is thus an effective reservoir management tool (e.g. Michelet & Toksöz 2007; Bromley 2014; Kaven *et al.* 2014). However, the potential risk of inducing larger earthquakes has raised public concern, since these events may be felt, and thus represent a nuisance, or in extreme cases may be strong enough to cause injuries and damage surface structures, and thus represent a hazard (e.g. Giardini 2009). Extensive reviews of seismicity related to injection activities in EGS and geothermal fields in general include the works by Majer *et al.* (2007) and Zang *et al.* (2014). According to Zang *et al.* (2014), local magnitudes of some of the largest seismic events associated with geothermal operations so far are a M_L 4.6 event at The Geysers (USA) in 1982, a M_L 4.4 event at the Berlin field (El Salvador) in 2003, a M_L 3.7 event in the Cooper Basin (Australia) in 2003 and a M_L 3.4 event in Basel (Switzerland) in 2006. Events of this size, at shallow depths, are strongly felt, the larger ones being around the threshold where minor damage might be expected.

These examples indicate that assessment and mitigation measures are needed to reduce the seismic risk from injection activities. Good-practice guidelines for risk assessment and induced seismicity management in geothermal projects have therefore been developed (Majer *et al.* 2012; Wiemer *et al.* 2017; Bohnhoff *et al.* 2018). These include selection of sites with low seismic risk and the application of seismic traffic light systems (TLS). Soft stimulation concepts have also been proposed as risk mitigation measures (Zang *et al.* 2013; Zimmermann *et al.* 2015; Huenges *et al.* 2017). Soft stimulation is defined as geothermal reservoir stimulation that aims to achieve enhanced reservoir performance while minimizing environmental impacts including induced seismicity (Brehme *et al.* 2017; Huenges *et al.* 2017). It includes techniques such as cyclic or fatigue (Zang *et al.* 2013), multistage (Meier *et al.* 2015), chemical and thermal stimulation (Huenges *et al.* 2017). In the framework of the European Commission funded Horizon 2020 project DESTRESS the cyclic soft stimulation concept has been applied for the first time at field

scale at the Pohang EGS project site in Korea to show its ability to limit the maximum magnitude of hydraulically induced seismic events.

Cyclic injection, with alternating phases of high and low flow rate, as opposed to conventional injection at constant flow rate, has been proposed as a soft stimulation concept after its potential advantages have been demonstrated by laboratory and mine-scale experiments and supporting numerical simulations and theoretical considerations (e.g. Zang *et al.* 2013, 2017a; Yoon *et al.* 2015a; Zhuang *et al.* 2016, 2017, 2018; Diaz *et al.* 2017, 2018; Patel *et al.* 2017; Stephansson *et al.* 2018). These advantages include a reduction in breakdown pressure, a reduced magnitude of the largest induced seismic event, and the development of more complex fracture networks compared to monotonic injection, while increasing the hydraulic performance of the system (Hofmann *et al.* 2018a; Zang *et al.* 2018). Similar benefits have been found from mechanical cyclic loading experiments (e.g. Cerfontaine & Collin 2017).

Many of the aforementioned studies have recommended controlled field experiments of the cyclic stimulation concept. However, to the best of our knowledge, cyclic injection has not previously been applied in a real field case with the aim of limiting the magnitude of induced seismic events. Previous intermittent injection has been for other operational reasons, not seismicity control. For example, a cyclic waterfrac treatment was performed at the Groß Schönebeck EGS site in Germany (Zimmermann *et al.* 2010). Even though seismic risk reduction was not the intention, it was observed that seismicity resulting from this treatment was very low (Kwiatk *et al.* 2010). This experience initiated the development of the cyclic soft stimulation (CSS) concept, which is described briefly here and which is explained more extensively elsewhere (Hofmann *et al.* 2018b).

At the Pohang EGS site in Korea different injection schemes were applied between 2016 and 2017, including constant rate injections and cyclic injection with shut-in. These treatments caused seismic events with magnitudes above 2.0 (Kim *et al.* 2017a). Two months after the last stimulation in September 2017, a M_w 5.5 earthquake occurred in the vicinity of the EGS site on 15 November 2017 (KMA 2018). Since then, the project is on hold. This event is of critical relevance for deep geothermal energy exploitation worldwide. Currently, several studies by different research groups and by a governmental commission are ongoing to investigate whether and how EGS site activities could be related to this earthquake (e.g. Dahm *et al.* 2018; Grigoli *et al.* 2018; Kim *et al.* 2018a). The first and only CSS experiment was performed at this site between 7 and 14 August 2017 in well PX-1. Preliminary hydraulic and seismic results of this treatment have been presented by Hofmann *et al.* (2017, 2018a) and Fokker *et al.* (2018a). Specific analyses of these data sets will be reported in separate, specialized publications. As part of this research programme, numerical models are being developed that aim to improve the understanding and interpretation of the acquired data (Farkas *et al.* 2017, 2018).

This paper provides an overview about the work performed in August 2017 and a summary of its results. The most important aspects of the Pohang EGS project site are summarized first, then the stimulation design is presented and the hydraulic and microseismic field observations are provided and discussed.

2 THE POHANG EGS PROJECT

The first EGS project site in Korea is located in the SE part of the Korean peninsula, north of the city of Pohang (Fig. 1). This government and industry funded project was launched in December 2010 by a consortium consisting of the site owner and operator Nexgeo, research institutes (the Korea Institute of Geoscience and Mineral Resources, KIGAM, and the Korea Institute of Civil Engineering and Building Technology, KICT), a university (Seoul National University, SNU) and industry partners (the steel company POSCO and geothermal developer Innogeo). A 103 °C temperature has been reported at 2250 m depth (Yoon *et al.* 2015b). The surface heat flow is 94 mW m⁻² in a nearby borehole (Lee *et al.* 2010); 28 °C km⁻¹ geothermal gradient in the granite (Kim & Lee 2007) thus gives a temperature of ~160 °C at ~4.3 km depth. The bottomhole temperature measured 3 d after drilling was ~140 °C. The site was originally expected to deliver >1 MW of electrical power after the drilling of two wells and reservoir improvements through stimulation (Lee *et al.* 2011; Song *et al.* 2015). After this proof-of-concept phase, further development was anticipated by drilling a third well and additional stimulation treatments (Song *et al.* 2015).

The geothermal reservoir is located beneath the Pohang Basin, a sedimentary basin of Miocene age, which formed as a result of oceanic spreading within the adjacent East Sea (e.g. Jolivet & Tamaki 1992). One of the principal right-lateral faults that formed the western margin of this extensional zone, the Yangsan Fault, strikes NNE–SSW, passing ~10 km west of the geothermal site (e.g. Kim *et al.* 2016). The structure and stratigraphy of this basin have been discussed in detail (e.g. Choi 2006; Son *et al.* 2015). The Pohang geothermal reservoir is in fractured granodiorite below ~2350 m depth, emplaced during the Permian (age ~260 Ma according to Lee *et al.* 2014), then metamorphosed by Mesozoic tectonic activity (see, e.g. Chough *et al.* 2000; Cough & Sohn 2010, for details). This granodiorite is covered by Cretaceous sediments and volcanic rocks and by Miocene tuff and semi-consolidated mudstone, the latter with thickness varying between ~200 m in the north to >400 m in the south (Lee *et al.* 2015; Park *et al.* 2017a; Fig. 2).

The EGS project began with exploration of the site, including examination of existing borehole records and multidisciplinary geophysical prospecting. A conceptual model for the site and its surroundings was thus developed (Lee *et al.* 2015; Park *et al.* 2017a). This model envisages the Pohang Basin as transected by a set of NNE–SSW striking faults, oriented subparallel to the Yangsan Fault, and subperpendicular conjugate faults or fractures. Mapped and inferred fault traces from this geological model are shown in Fig. 1.

Integrated *in situ* stress measurements in a 1002 m deep nearby borehole indicate a maximum horizontal stress direction between N130°E and N136°E in a strike-slip stress regime (Kim *et al.* 2017b). Extrapolation of this stress model to 4278 m depth results in maximum, intermediate and minimum principal stresses of 139, 110 and 82 MPa, respectively. However, a comparison between deep and shallow stress field measurements in Korea shows significant variations in stress field directions in SE Korea, possibly due to local geological structures (Lee *et al.* 2016); other researchers have also determined different orientations and stress states for this area (Park *et al.* 2006).

Well PX-1 was drilled in 2012/2013 and side-tracked in 2016 to a measured depth of 4362 m and a true vertical depth of 4215 m, with an 8 1/2" diameter openhole section of 313 m length at its bottom. This well has been completed with a 9 5/8" casing to 2400 m depth and a 7" casing from 2400 to 3920 m TVD (4049 m MD), the remainder being left openhole (Fig. 2). The well is deviated by 22°

towards an azimuth of 289°. The vertical well PX-2 was drilled and completed in 2015 down to 4348 m, with a 7" casing down to 4208 m and a 140 m long 8 1/2" diameter openhole section (Fig. 2). At the surface the wells are 6 m apart; the well bottoms, as ultimately completed, are separated by 616 m. Extensive characterization has been performed on 3.6-m-long rock core extracted at 4.2 km depth of PX-2 (Kwon *et al.* 2018).

Before the CSS treatment, three hydraulic stimulations were performed to improve the hydraulic performance of the system. Well PX-2 was stimulated in January 2016 and March/April 2017. Well PX-1 was stimulated in December 2016. In PX-1 hydro shearing was inferred as the primary stimulation mechanism, occurring at relatively low wellhead pressures (WHP) of ~16 MPa, in agreement with a prediction using the model stress field (Park *et al.* 2017b). In contrast, PX-2 showed much lower injectivity than PX-1, without clear indication of hydraulic shearing, requiring higher injection pressure up to 89 MPa (Park *et al.* 2017a). The local magnitudes of the largest induced seismic events caused by these treatments were M_L 2.3 for PX-1 (Kim *et al.* 2017a; KMA 2018) and M_L 3.1 for PX-2 (Grigoli *et al.* 2018; KMA 2018). This history of induced seismic events above magnitude 2.0 accompanying fluid injection meant that further development required a soft stimulation approach, which was subsequently designed for well PX-1 and is the subject of this manuscript.

3 STIMULATION DESIGN

The spatial distributions of the seismic clouds that developed during the previous three hydraulic stimulations have not clearly been identified by the time these stimulations were completed, which has made it difficult to take measures to improve the hydraulic connection between the two wells. Furthermore, the largest induced earthquake, of M_L 3.1 occurred shortly after the third hydraulic stimulation, which has been carried out in PX-2. Therefore, the fourth hydraulic stimulation, introduced in this study, focused on improving the location of seismic clouds, much attention being paid to limiting the seismicity to moment magnitudes $M_w < 2.0$. In detail, the objectives of this treatment were, listed according to priority from high to low: (1) to test the cyclic soft stimulation concept in the field; (2) to inject fluid without inducing seismic events of $M_w \geq 2.0$; (3) to map the stimulated reservoir volume as potential future drilling target; (4) to monitor the stimulation performance in real time using harmonic pulse test analysis and (5) to increase the hydraulic performance of the system. The treatment schedule and monitoring system were tailored for these purposes.

3.1 Cyclic soft stimulation concept

The CSS concept consists of cycles with high-rate and low-rate injection of roughly equal duration. The cycles can be of three different timescales with different objectives (Fig. 3).

The application of short-term cycles is based on the concept of fatigue hydraulic fracturing (FHF), introduced by Zang *et al.* (2013, 2017b, 2018), whereby pressure pulses are intended to weaken ('fatigue') the rock by inducing microcracks before macroscopic failure. This has three major intended benefits. First, the stimulated reservoir volume is increased due to more complex fracture growth. The resulting stimulated fracture network thus provides a larger heat exchanger area. Second, the breakdown pressure is reduced. Therefore, lower injection pressures are required to stimulate the target formation and lower pressures may reduce the potential for slip on

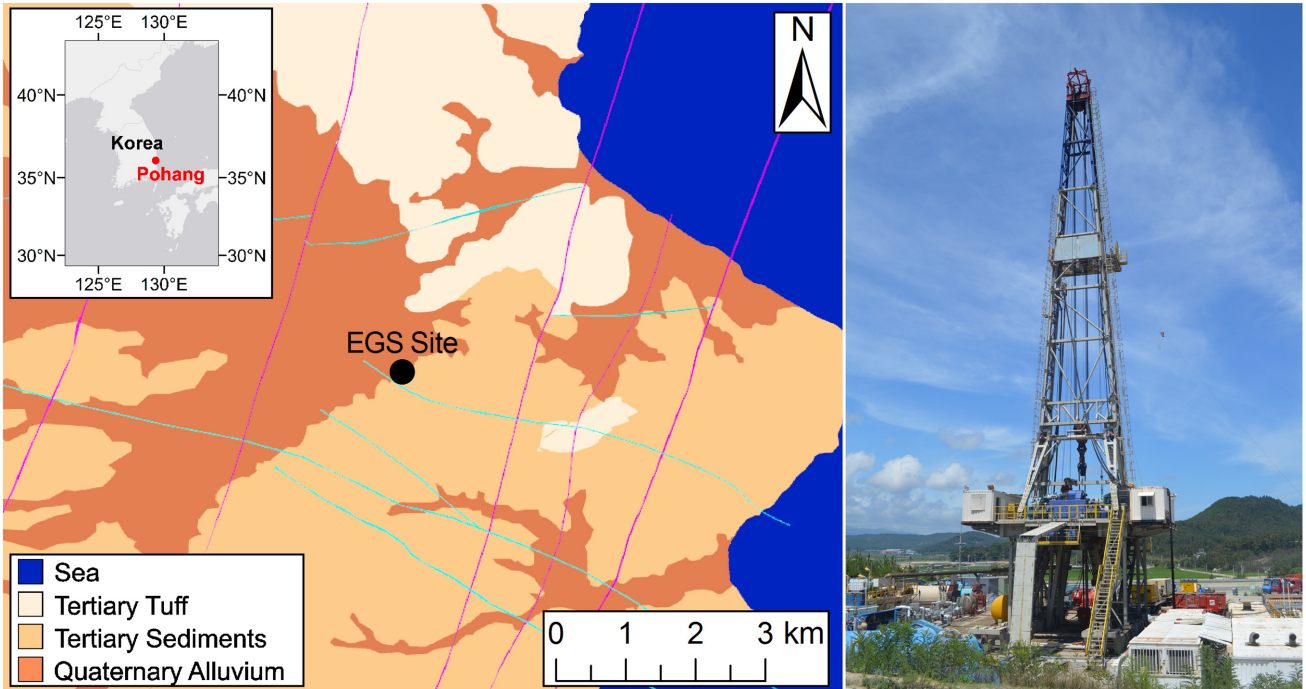


Figure 1. Pohang EGS project location, surface geology, inferred surface faults (left-hand panel) and view of the site (right-hand panel).

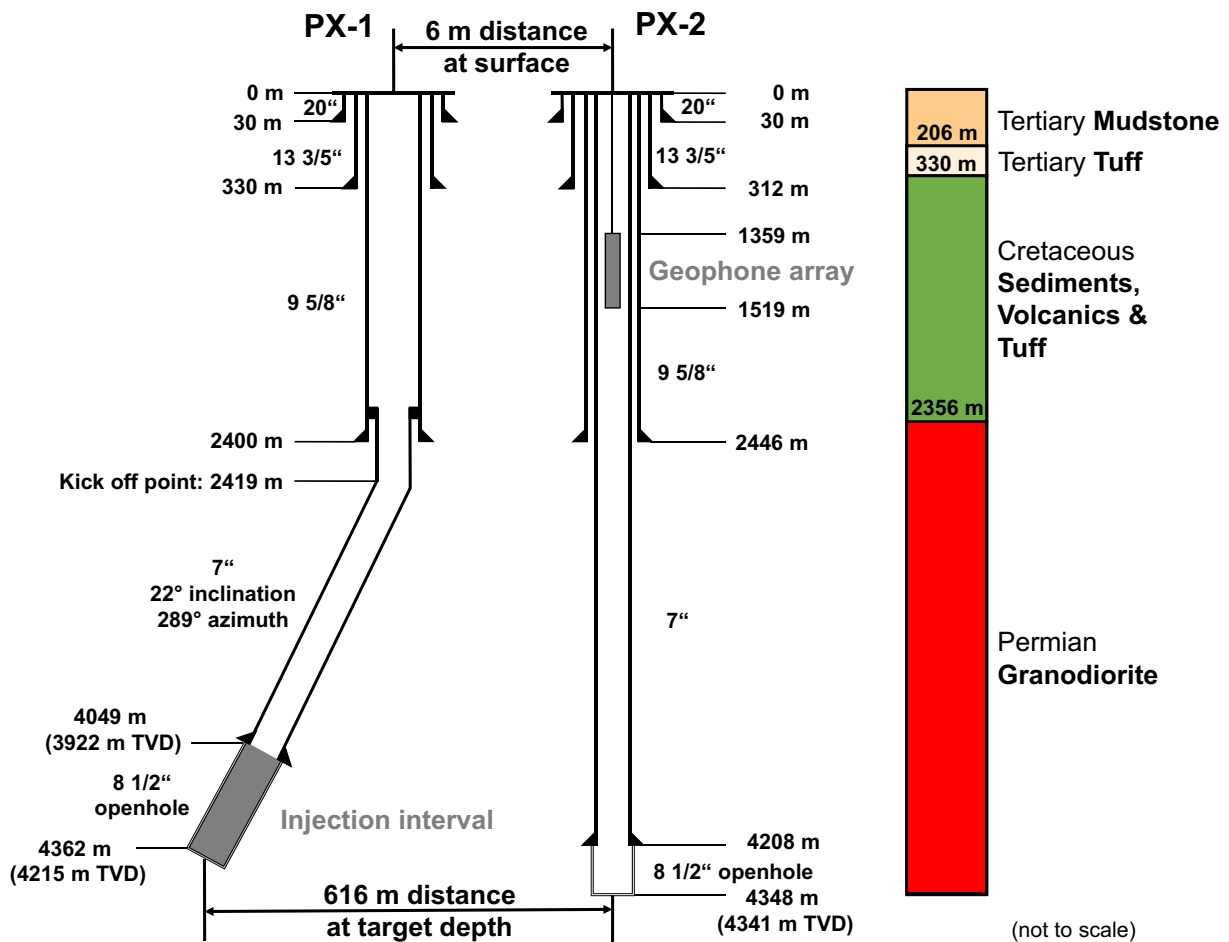


Figure 2. Well completions including injection location (PX-1, 313 m long openhole section from 4049 to 4362 m MD) and 17-instrument geophone chain (installed in well PX-2, at 1359–1519 m MD, to monitor the August 2017 stimulation in well PX-1). Depth reference is the rig floor, 26.3 m above sea level and ~9 m above surface.

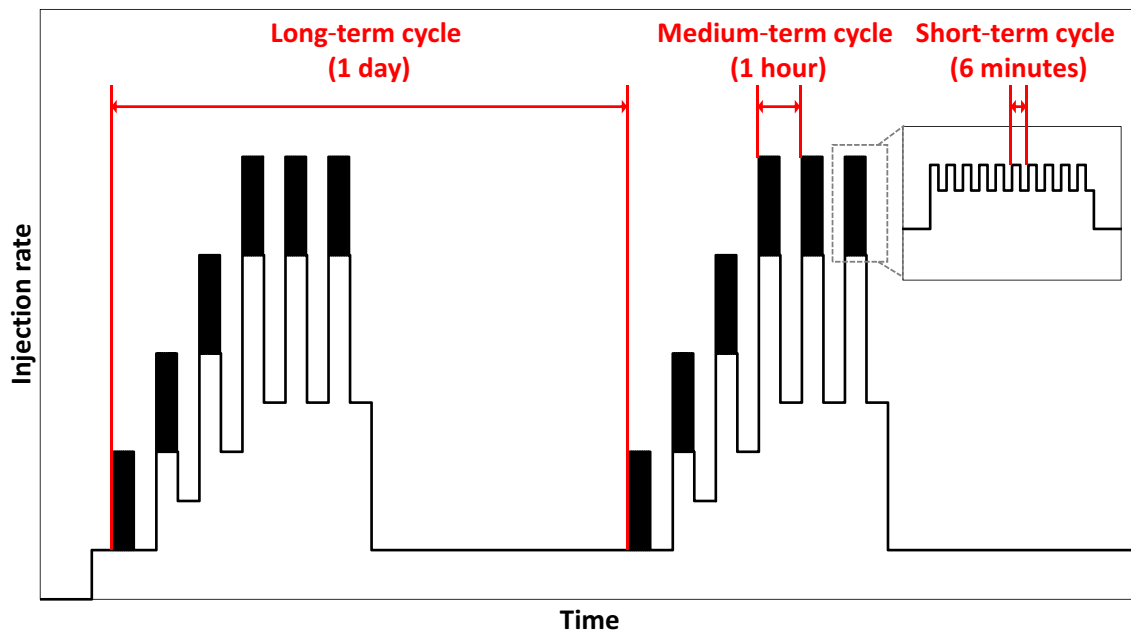


Figure 3. Summary illustration of the cyclic soft stimulation concept with long-, medium- and short-term cycles used in August 2017 in well PX-1 at Pohang.

faults and thus the likelihood of induced seismic events. Third, the magnitude of the largest induced seismic events is reduced.

In addition to the above, medium-term cycles divide the amount of hydraulic energy introduced into the subsurface into small parts as compared with continuous injection. This aims to stimulate the fracture network stepwise.

Long-term cycles are applied because of the common observation that seismic events occur after a delay following the actual fluid injection. The long phase with reduced flow rate is intended to slowly reduce the reservoir pressure to a level where the activated fracture system is closed. During this time the stresses introduced into the system can be redistributed. This occurs on a very short timescale due to poroelastic stress redistribution and on longer timescales, depending on the diffusivity of the system, due to fluid flow. Additionally, this procedure gives the operator time to observe the seismic reaction of the system to the hydraulic injection, including any relatively large magnitude seismic events, and to adapt the injection schedule accordingly.

In general, flow rates progressively increase during each medium-term cycle until fracture opening is observed. From this point on the same medium-term cycle is repeated until the end of the long-term cycle. This is needed to keep the treatment pressures as low as possible, but as high as necessary. Additionally, this procedure allows re-evaluation of the fracture opening pressure at the start of each long-term cycle. Using this information, the flow rates can be adjusted. This mode of operation also ensures that the condition for reservoir stimulation is approached slowly. Since the largest seismic events sometimes occur during shut-in (e.g. Deichmann & Giardini 2009; Baisch *et al.* 2010; Park *et al.* 2017a), and in order to apply slow pressure changes, the CSS concept envisages no shut-in phases, but low base rate injection or flowback instead. To allow for the possibility of flowback, sufficient storage and transportation capacity has to be ensured at the site before the treatment. A more detailed explanation of this CSS concept is reported elsewhere (Hofmann *et al.* 2018b).

3.2 Injection scheme

The injection scheme for the Pohang CSS treatment in August 2017 was based on the concept described above and on available data from previous stimulations. Overall, the maximum allowable injection volume was limited to 2000 m³. This was based on the observation, from the previous treatments at Pohang, of a systematic trend between injected net fluid volume and the magnitude of induced seismic events, given the maximum anticipated magnitude of 2.0. Larger fluid volumes would predict larger magnitudes based on this trend.

The maximum flow rate was limited to 10 l s⁻¹, since fracture opening had already occurred at lower flow rates during the previous stimulation of well PX-1. Based on the previous pressure responses, the maximum WHP was limited to 25 MPa, sufficient to stimulate the reservoir, but <10 MPa above the opening pressure observed during the previous stimulation. The long-term cycle length was chosen to be 1 d based on the previously observed delays between injection and seismic response. Medium-term cycles were of 2-hr length and short-term cycles 6 min, short enough to allow sufficient numbers of cycles for harmonic pulse testing analysis, but long enough for real-time injectivity determination. The lowest possible base flow rate was 1 l s⁻¹ due the specifications of the injection pumps. Based on these parameters, the maximum duration of stimulation was originally planned to be 10 d.

After an initial 3 d of injection tests, at least 1 d of shut-in was planned, followed by multiple long-term cycles during the main stimulation phase, a slow pressure decrease after stimulation, ending with post-stimulation injection tests. The initial injection tests were intended to determine the initial hydraulic performance, fracture opening pressure and seismic response. The shut-in phase before the main stimulation treatment was intended to observe the seismic response, judge the risk of further injection and adapt the main treatment schedule. The injection tests after the main treatment were intended to determine the change in hydraulic performance resulting from the stimulation treatment.

3.3 Hydraulic system setup

The stimulation fluid was water from an irrigation reservoir 300 m from the site. It was pumped through a 180 μm filter to water tanks on site, the total capacity of tanks and mud-pit being $\sim 1000 \text{ m}^3$. As well as storing injection water, these tanks were used to collect water produced during flowback. One of two mud pumps, with a minimum stable flow rate of $\sim 1\text{--}2 \text{ l s}^{-1}$, was used for injection while the other was available as a backup. The injection rate, calculated from the pump efficiency and the number of pump strokes per minute, was recorded every 2–3 s. An approximation of this real flow rate was also provided in real time every second.

Pressure was measured directly at the wellhead (i.e. wellhead pressure, WHP) with a reading precision of 0.1 MPa and recorded every second. Additionally, the stand pipe pressure (SPP) on the rig was measured every 2–3 s. The SPP was ~ 1 MPa higher and much more prone to variation compared with the WHP and was therefore not used for the analysis. Flowback rates and volumes were calculated by measuring the water level in the water tanks or in the rig cellar at defined intervals. During flowback periods the water was stored on site and transported away by trucks at regular intervals for treatment and disposal. Before, during and after the stimulation, water samples were taken and water properties were measured on site; analysis and modelling of the changes in the hydrochemistry of this produced water, as a result of its residence within the reservoir for variable intervals of time, will be published separately.

3.4 Seismic real-time monitoring and traffic light system

The seismic monitoring system deployed in August 2017 (Fig. 4) consisted of a 17-instrument three-component borehole geophone array deployed in well PX-2 at 1350–1510 m measured depth (MD) below surface with 10 m spacing between instruments (Fig. 2), four three-component surface velocity meters (MSS01–4), nine three-component borehole sensors (PHBS01–8 + EXP01), and a borehole accelerometer at a depth of 2380 m in the deep borehole BH-4. All these stations were distributed within ~ 7 km around the site (Fig. 4). The geophone array in well PX-2 was in operation from 26 July 2017 until 23 August 2017; the other stations formed a permanent monitoring network for the site.

Only the surface station MSS01 was directly connected to lithified bedrock (the Early Miocene tuff; Fig. 1) and thus had a satisfactory signal to noise ratio. It is also one of few stations that was continuously operational during previous stimulations. During that time, station MSS01 recorded four events for which the Korea Meteorological Administration (KMA), the Korean government agency responsible for monitoring seismicity, reported magnitudes $M_L \geq 2.0$, their official reporting threshold. Both aspects made this station an ideal candidate to equate locally measured peak ground velocity (PGV) values against KMA local magnitudes, using these four events. The PGV value measured at station MSS01 was therefore used as trigger for a real-time alerting system during the August 2017 stimulation.

Once a PGV trigger level of $\geq 10 \mu\text{m s}^{-1}$ was detected at station MSS01 by this alerting system, an automatic email was sent to the team members and the location and moment magnitude M_w were manually determined using all available stations. The operations were then adapted based on this moment magnitude, using the seismic traffic light system shown in Fig. 5. To avoid false alarms based on noise triggers an email would only be sent in case the more sensitive downhole geophone array in well PX-2 was also triggered.

Functionality was guaranteed by continuous manual surveillance. The geophone array was in operation from 26 July 2017 until 23 August 2017.

A traffic light system, such as this, can be an effective tool to mitigate induced seismic events above a given threshold. At Pohang, an existing traffic light system (Kim *et al.* 2018b) was adapted for CSS by including different action items for events during high-rate injection phases or during low-rate or base rate injection. Actions include specifying, for each threshold level of the traffic light system, adjustments to injection rates during the following long-term cycle. Since the target was to keep seismicity below M_w 2.0, this was the threshold for stage 5 of the traffic light system. According to the TLS described by Kim *et al.* (2018b), a magnitude difference of $\Delta M_w = 0.3$ between the stages was used except for Stage 2 with $\Delta M_w = 0.4$. This is reasonable based on the observation that during most of the past stimulation in well PX-1 in December 2016, before the deviation from this trend at around 3600 m^3 injected net volume (V_{net}), the magnitude of an event was never higher than 0.3 compared to the previous largest event. Assuming this observation would be valid also for forthcoming stimulations, appropriate actions according to the TLS could thus be taken before magnitudes increase significantly above the target level. In the descriptions that follow, concerning site operations and associated induced seismicity, all events are reported in Korean standard time (KST), which is 9 hr ahead of GMT.

The traffic light system procedures used for the August 2017 CSS treatment at the Pohang EGS site are described below and summarized in Fig. 5.

Stage 1–green ($M_w < 1.0$): The treatment continues as planned. This is independent of the injection phase in which the event occurs. During the following long-term cycle the same schedule can be repeated or the injection rates may be increased depending on the required flow rates and pressures to open the fractures. This is decided based on the pressures measured on the previous day.

Stage 2–yellow ($1.0 \leq M_w < 1.4$): If the event occurs during a high rate phase, the flow rate is reduced to what it was during the previous high rate phase, and subsequent high rate phases during that long-term cycle are also limited to the same injection rate. If the event occurs during base rate injection, no further high rate injections will be performed during the current long-term cycle. During the following long-term cycle, the maximum injection rate is limited to the maximum injection rate before the seismic event occurred.

Stage 3–orange ($1.4 \leq M_w < 1.7$): If the event occurs during high rate injection, the flow rate is reduced to the base rate and it is not increased again during the current long-term cycle. If the event occurs during low rate injection, the rate is reduced to the minimum possible base rate. During the following long-term cycle, the flow rate is kept at this base rate and no high rate injection cycles are performed. If a stage 3 event occurs during injection at the lowest base rate, flowback is initiated.

Stages 4 and 5–red ($1.7 \leq M_w < 2.0$ and $M_w \geq 2.0$): Irrespective of the injection phase in which the event occurs, flowback is initiated, to minimize the possibility of further events with higher magnitudes. Once flowback is initiated, irrespective of whether because of a stage 3, 4 or 5 event, it proceeds to completion. Subsequent injection may only occur after an updated risk assessment in the light of the new data. Despite the same action items, a distinction between Stage 4 and 5 was made to highlight the additional margin of safety of $\Delta M_w = 0.3$, to distinctly show the magnitude that is to be avoided in the TLS (M_w 2.0), and to differentiate the stages for internal reporting purposes.

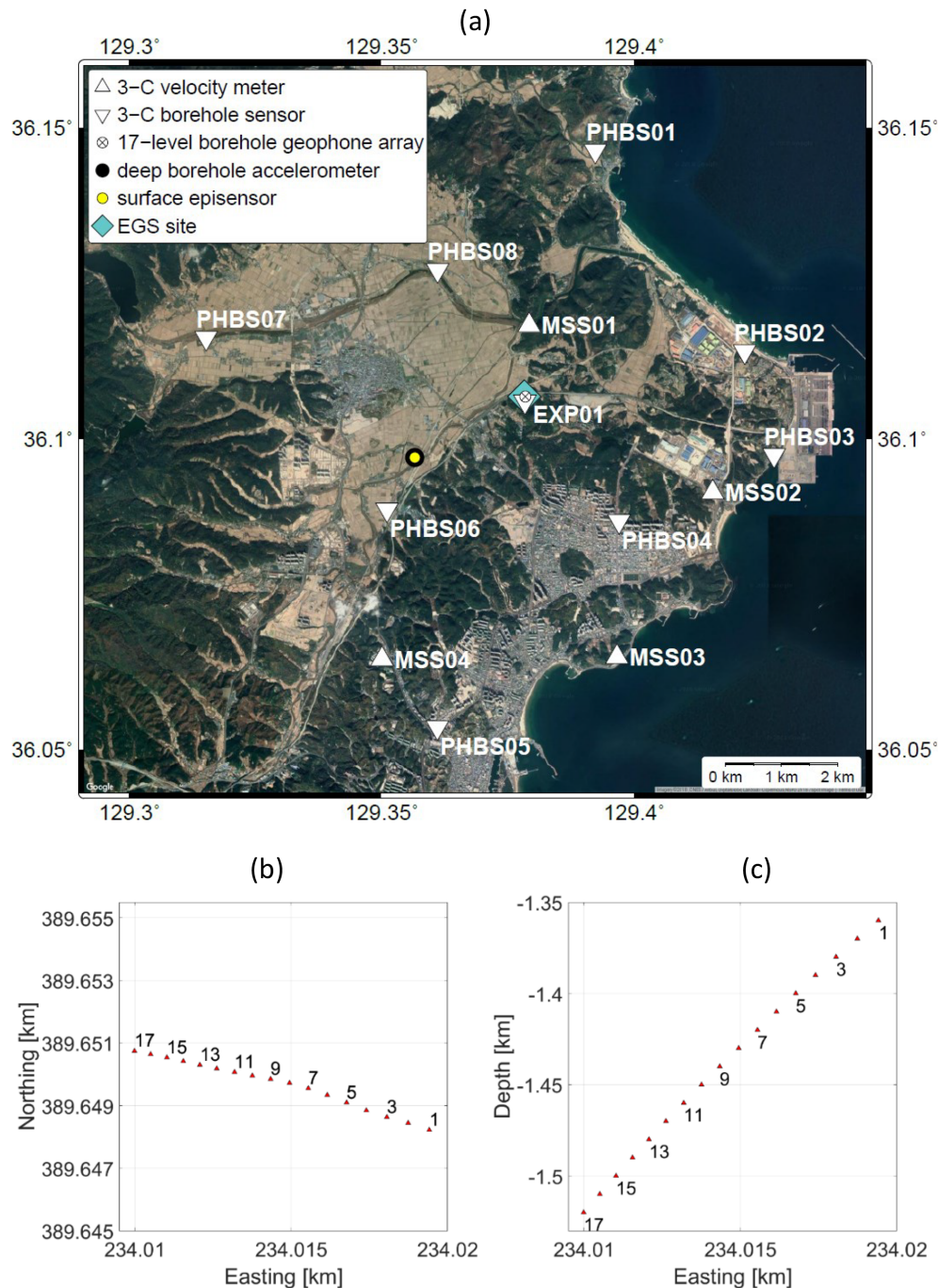


Figure 4. Seismic monitoring instrumentation. (a) The seismic monitoring network during the cyclic soft stimulation in August 2017 consisted of a permanent monitoring network for the site, comprising four three-component (3-C) surface velocity metres (MSS01–4), nine 3-C borehole sensors (PHB01–8 and EXP01), and a borehole geophone in well BH-4, supplemented for this particular stimulation by a 17-instrument 3-C geophone array in well PX-2. (b) and (c) Geometry of the geophone array. This was slightly inclined to the WNW as shown by this plan view and cross-section of the sensor locations.

Events detected by the alerting system were located and seismic moments (M_0) and moment magnitudes (M_w) were determined in real time. These determinations used unfiltered seismograms (corrected for instrumental response), assuming a seismic velocity model and quality factor for anelastic attenuation, Q_s , of 300, based on experience from previous stimulations. A single value for M_0 was determined for all seismograms used, then M_w was calculated

following Hanks & Kanamori (1979) and Bormann & Di Giacomo (2011):

$$M_w = \frac{2}{3} (\log_{10} M_0 - 9.1). \quad (1)$$

The resulting M_w values were used to implement the TLS.

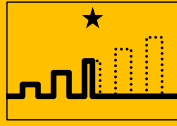
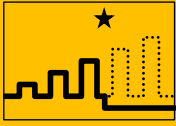
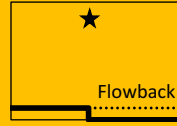
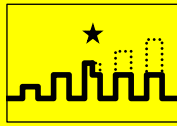
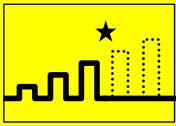
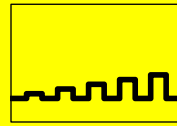


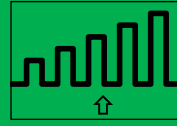
PGV ($\mu\text{m/s}$) @ MSS01	M_w	Stage	Injection rate (Event @ high rate)	Injection rate (Event @ low rate)	Adjusted injection rates for next cycle
≥ 100	≥ 2.0	5	Flowback	Flowback	Flowback
≥ 52	≥ 1.7	4	Flowback	Flowback	Flowback
≥ 27	≥ 1.4	3			
≥ 10	≥ 1.0	2			
< 10	< 1.0	1			
Legend: ★ Induced seismic event — adjusted injection rate ... planned injection rate					

Figure 5. Seismic traffic light system (TLS) used for the cyclic soft stimulation treatment in well PX-1 in August 2017. The magnitude thresholds were converted to peak ground velocity (PGV) values recorded at surface station MSS01. Measured PGV values were used as the triggering parameter for alerts, then magnitudes were determined as M_w and used to implement the appropriate response from the TLS. Stage 5 defines the maximum magnitude that is to be avoided and shows the margin of safety of $\Delta M_w = 0.3$.

3.5 Hydraulic data analysis

Multiple methods were considered to analyse the hydraulic data set, consisting of measurements of flow rate and WHP. As a first order real-time analysis, the variations in flow rates and WHP were logged.

A second standard approach would be to monitor changes to the injectivity index (II) of well PX-1. The II is defined as the ratio of injection rate and the difference between the bottomhole flowing pressure under steady-state conditions and the undisturbed reservoir pressure (Economides & Nolte 2000). However, this conventional definition of II could not be used in the present analysis because only the WHP was measured directly and because steady-state conditions were not reached during the relatively short constant injection rate phases of the individual cycles.

Analysis methods undertaken include monitoring of changes to dynamic injectivity, conventional well test analysis, and harmonic pulse testing.

3.5.1 Dynamic injectivity development

The dynamic wellhead injectivity index (DWII) was calculated using the flow rate q_2 and wellhead pressure WHP_2 at the end of each intermediate high rate cycle and the initial wellhead pressure WHP_0

before the treatment (Messer, Pye, & Gallus 1978):

$$DWII = \frac{q_2}{WHP_2 - WHP_0} \tag{2}$$

In addition to this, the dynamic differential wellhead injectivity index (DDWII) was calculated using the injection rates q_1 and q_2 and the wellhead pressures WHP_1 and WHP_2 at the start and end of each high rate phase, respectively:

$$DDWII = \frac{q_2 - q_1}{WHP_2 - WHP_1} \tag{3}$$

As in previous applications (Garg & Combs 1997; Pasikki *et al.* 2010; Grant *et al.* 2013), this differential injectivity was used to account for the changing conditions during the various cycles. For phases with short-term injection cycles, the average flow rate during short-term cycling was used. The fracture opening pressure was determined by identification of a distinct reduction of the gradient of the variations of WHP with flow rate q during progressively increasing flow rates (e.g. Huenges *et al.* 2006).

3.5.2 Conventional well test analysis

The fall-off sequences (shut-in periods) and flowback (production) during and after the stimulation treatment were analysed using classical well test analysis (Horne 1995). The evolution

of transmissivity and permeability is thus calculated from pressure decline curves after each injection stage, taking into account the superposition principle and assuming infinite-acting radial flow. The calculations are based on the generalized formula for pressure (p) development with stepwise flow rate (q) changes (Lee 1982):

$$p(r, t) = p_0 + \sum_{i=1}^n \frac{(q_i - q_{i-1})\mu}{4\pi k h} \times \left(0.5772 + \ln \left(\frac{\Phi \mu c_t r^2}{4k(t - t_{i-1})} \right) - 2s \right), \quad (4)$$

where r is the well radius, p_0 is the initial pressure, c_t is the total compressibility, s is the skin, t is the total time, t_i is the interval time, h is the interval length, q_i is the interval flow rate, k is the permeability, μ is the dynamic fluid viscosity and Φ is the porosity. The transmissivity kh is calculated from the logarithmic superposition time derivative of the pressure decline curve after Lee (1982):

$$\frac{\partial(\Delta p)}{\partial \left(\ln \left(\frac{t_s}{t_s + t_p} \right) \right)} = \frac{q\mu}{4\pi k h}, \quad (5)$$

where t_s is the shut-in time and t_p is the injection time.

The productivity index PI is calculated two ways for comparison. The first is the pseudo steady-state solution of Lee (1982):

$$PI = \frac{q}{\Delta p} = \frac{2\pi kh}{\mu} \frac{1}{\ln \left(\frac{R}{r} \right) - 0.75 + s}, \quad (6)$$

where R is the radius of the reservoir (no-flow boundary). The second uses the solution for a doublet system with injection and production wells:

$$PI = \frac{q}{\Delta p} = \frac{2\pi kh}{\mu} \frac{1}{\ln \left(\frac{d}{r} \right) + s}, \quad (7)$$

where d is the distance between injection and production well.

3.5.3 Harmonic pulse testing analysis

In harmonic pulse testing (HPT) a train of equal-duration pulses in injection rate or production rate is applied to a reservoir. The pressure is monitored in the injection well ('pulsar well'), or in a nearby observer well. With a fast Fourier transform (FFT) algorithm, frequency information can be extracted from these variations over time, as shown in Fig. 6. The interpretation of the different frequency components involves the evaluation of the pressure response to the rate input. The response has two components: the amplitude quantifies how large the absolute value of the response is with respect to the input; the phase quantifies the delay of the response relative to the input. Fokker *et al.* (2018b) have derived theoretical expressions for these quantities in terms of model parameters, including transmissivity, skin, well-bore storage and reservoir storativity, which can be matched against observations.

In comparison to well testing, pulse testing employs a number of pulses rather than a single one. Therefore, it has the disadvantage of requiring more time, but the advantage that it can be used during injection or production operations, by superposition of pulses onto an injection or production schedule, to monitor the development of hydraulic parameters. The pulsed injection schedule into well PX-1 in August 2017, adopted primarily for other reasons, facilitated this analysis.

3.6 Seismological data analysis

3.6.1 Compilation of seismicity catalogue

During and shortly after the August 2017 stimulation treatment 52 seismic events were detected in real-time. In addition to the real-time analysis already described, further analysis was subsequently carried out, as described here, to refine the source parameters of these events. While all events were clearly recorded on all sensors of the borehole geophone array, only a few events were detected by the surface and shallow borehole stations, mainly due to their limited signal-to-noise ratios (SNR). Therefore, only the borehole geophone array was used for the present analysis.

In addition to the recorded direct P - and S -waves, another signal following every event and characterized by distinct two-phase arrivals was observed on sensors of the borehole geophone array in well PX-2 (Fig. 7). The move-out of these post P - and S -phase onsets suggests a velocity across the array of $\sim 1500 \text{ m s}^{-1}$ for both phases. These phases are thus interpreted as tube waves travelling along well PX-2. A tube wave is a body wave which travels from an external source to a receiver well and gets converted at a borehole (e.g. Mo & Harris 1995; Wu & Harris 2004). In our case both the P - and S -waves are converted into tube waves at the openhole section of well PX-2, and then travel along this well towards the geophone array at the P -wave velocity in the borehole fluid ($\sim 1500 \text{ m s}^{-1}$); the phases of these tube waves are a converted P - wave (PT) and a converted S -wave (ST), respectively (Fig. 7).

For this re-analysis we filtered the seismograms with second order high-pass Butterworth filters with cut-off frequencies tied to the event magnitude. We then manually re-picked P -, S -, PT- and ST-wave onset times on all available three-component seismograms.

3.6.2 Location and magnitude estimation

The re-picked seismic phase onsets were inverted for hypocentre locations using the Equal Differential Time (EDT) method (Zhou 1994; Font *et al.* 2004; Lomax 2005). The predicted arrival times were modelled assuming a 1-D layered velocity model with P - and S -wave velocities for the deepest layer of $V_p = 5845 \text{ m s}^{-1}$ and $V_s = 3305 \text{ m s}^{-1}$, respectively, as had been refined for use during the previous stimulations. We have assumed that the conversion to tube waves occurs at the top of the open-hole section of well PX-2, at 4208 m depth. The typical $\sim 0.06 \text{ s}$ arrival-time differences between the PT- and ST-phases (Fig. 7) indicate that most of the seismic events occurred $\sim 500 \text{ m}$ away from this point.

The difference between the modelled arrival times ($T_{i,j}^{th}$) was then compared with the difference of observed arrival times ($T_{i,j}^{obs}$), leading to the following inverse problem:

$$\| (T_j^{th} - T_i^{th}) - (T_j^{obs} - T_i^{obs}) \|_{L_2} = \min. \quad (8)$$

The norm in eq. (8) was calculated using all unique pairs (i, j) of P -, S -, PT- and ST-wave onset times. The cost function on the left hand side of eq. (8) was sampled 1 million times using the Metropolis-Hastings Random Walk sampling algorithm (MHRW; Metropolis *et al.* 1958; Hastings 1970). The hypocentre selected corresponds to the minimum of the cost function. The ensemble of hypocentres sampled by MHRW was used to calculate the 3-D likelihood function and to characterize location uncertainty. The reliability of hypocentre locations was evaluated using the root mean square (RMS) difference between predicted and observed arrival times.

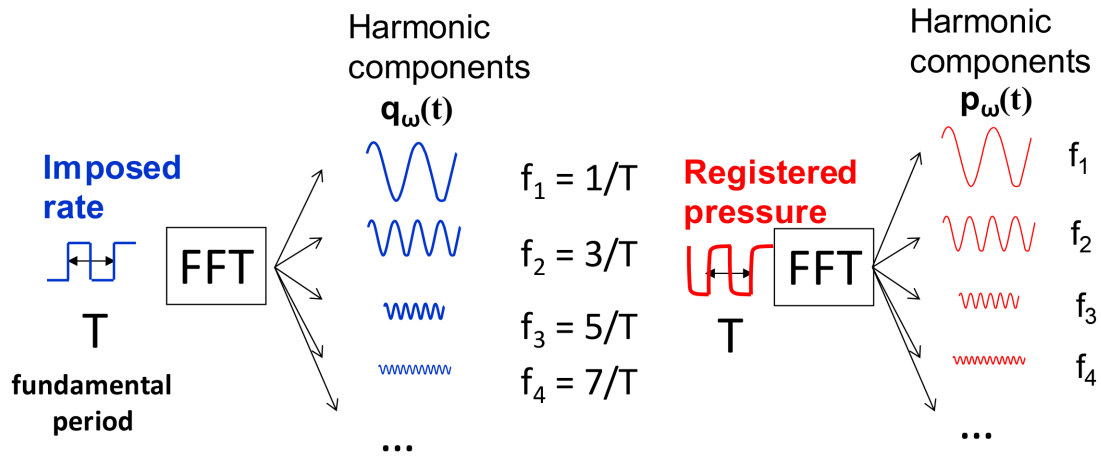


Figure 6. Principle of harmonic pulse testing. In summary, a flow rate variation consisting of a series of pulses is decomposed into separate Fourier components. The pressure responses for each of the Fourier components are summed, and the resulting synthetic pressure pulses matched against observations to determine hydraulic properties.

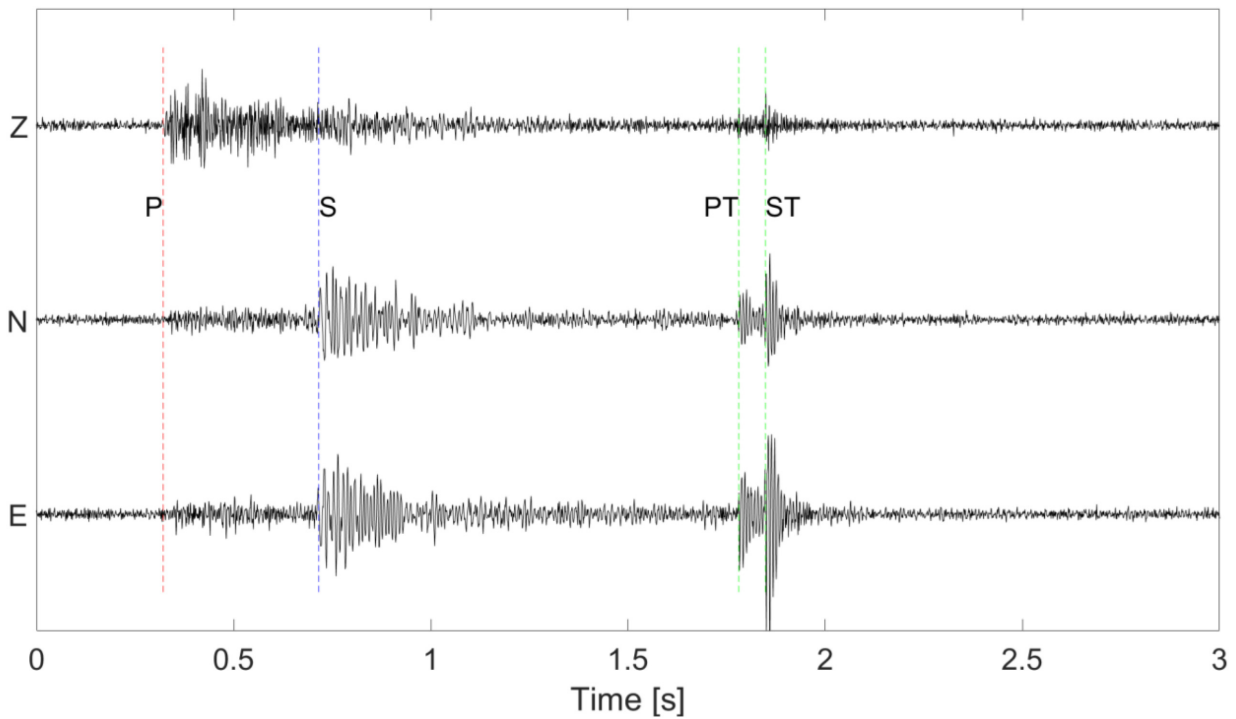


Figure 7. Three-component seismogram with onsets of direct P -wave and S -wave as well as tube wave phases PT and ST from one of the borehole array instruments for an event which occurred on 13 August 2017 at 21:46.

For magnitude estimation, we preprocessed the waveforms of the events focusing on the S -wave onsets, the most energetic part of the waveform. The frequency spectra of all channels from the borehole geophone array were first corrected for instrument response. The three-component seismograms were then analysed using a window length of 512 samples including 32 samples before the S -wave onsets. The windows were smoothed using a von-Hann taper. Ground displacement Fourier spectra were then calculated for each station using these three-component recordings and combined after Abercrombie (1995).

S -wave ground displacement spectra with sufficient SNR were then modelled using the Boatwright (1978) point-source model. We assumed an average radiation pattern correction coefficient $R_s = 0.63$ (Boore & Boatwright 1984), a S -wave velocity of

$V_s = 3300 \text{ m s}^{-1}$ in the source area of the events and a density of $\rho = 2700 \text{ kg m}^{-3}$. Matching of logarithms of the modelled and observed spectra used the L_2 norm. This inversion problem was optimized using the Simplex algorithm (Nelder & Mead 1965; Lagarias *et al.* 1998). To calculate the starting model for Simplex optimization, we used the J and K integrals (Andrews 1986; Snoke 1987). The bounds for these integrals were set based on SNR to account for the finite frequency bandwidth of our observations (e.g. Di Bona & Rovelli 1988).

The initial seismic moment M_0 , corner frequency f_s and quality factor Q_s were (Snoke 1987):

$$M_0^{(\text{start})} = 2 \left(\frac{K^3}{J} \right)^{\frac{1}{4}}, \quad f_s^{(\text{start})} = \frac{1}{2\pi} \left(\frac{J}{K} \right)^{\frac{1}{2}}, \quad Q_s = 200, \quad (9)$$

The value $Q_s = 200$ was selected by comparing observed high-frequency spectra fall-off, corrected for attenuation, with the f^{-2} dependence expected for Boatwright's (1978) source model. We focused on a reliable determination of the seismic moment M_0 , which is only weakly sensitive to attenuation, from which M_w was calculated for each station using eq. (1). Finally, average values for M_0 and M_w for each event were calculated from the values obtained for individual instruments, following García-García *et al.* (1996).

4 RESULTS

4.1 Hydraulic and seismological field observations

Fig. 8 shows the WHP, injection rate, injected net volume and moment magnitudes of the seismic events detected in real-time during all phases of the CSS treatment.

4.1.1 Initial injectivity determination (7 August 2017)

At the start of the first injection, 1495 m³ of previously injected water was still in the reservoir. The initial water level was at wellhead level and there was no overpressure due to airlift tests performed in the days before the start of injection, after which the well was filled with water again to the wellhead level.

The first day was used to carry out a series of hydraulic tests to determine the initial reservoir conditions (Fig. 9). These included a 2-hr continuous injection with the lowest possible rate of 1 l s⁻¹ and subsequent shut-in, followed by a 2-hr continuous injection at 3 l s⁻¹ with 2-hr shut-in afterwards. In addition to this, eight 1-hr cycles with alternating periods of 30 min of 3 l s⁻¹ injection and 30 min of shut-in were performed for comparison with the conventional 2-hr injection test. At the end of the day, ten 6-min cycles with the same flow rates were performed as a base line measurement for later pulse tests at different pressure levels. The maximum WHP reached 4.1 MPa at the end of the last test; 74 m³ of water was injected and no seismicity was observed.

4.1.2 Fracture opening pressure determination (8 August 2017)

On the second day a modified step rate test (progressive cyclic injection test) was performed to determine the fracture opening pressure (Fig. 10). Therefore, seven 2-hr cycles were performed using a 1 l s⁻¹ base injection rate and progressively increasing high rate phases, starting with 2 l s⁻¹ and increasing in 1 l s⁻¹ steps to 8 l s⁻¹. Afterwards, injection continued at base rate level. The maximum WHP of 18 MPa was reached in the last cycle and no seismicity was observed. Before the start of the next injection test a total water volume of 272 m³ had been injected.

4.1.3 Hydraulic pulse tests (9 August 2017)

On the third day a repetition of the second day was performed, with pulses on top of the high rate injection (cyclic progressive pulse test). This was to enable a direct comparison of a pulse test with a test without pulses and to determine the changes to the hydraulic parameters with increasing flow rates using the hydraulic pulse testing analysis. The flow rates during the pulses were 1 l s⁻¹ above and below the rates of the cyclic progressive test of Day 2 to ensure the same injected volume and average injection rate during all cycles in both tests (Fig. 10). The highest injection rate on Day 3 was therefore 9 l s⁻¹. Injection was continued at the 1 l s⁻¹ base rate

until 07:00 the next morning to ensure a pressure reduction phase with a similar length as the previous test. The wellhead pressure reached 18.1 MPa and, again, no seismicity was observed. In total 473 m³ of water had been injected before the start of the following phase.

4.1.4 Shut-in (10 August 2017)

After the initial injection tests the well was shut-in for 24 hr to observe the hydraulic and seismic behaviour of the system during shut-in and to allow time for adaptation of the main stimulation treatment based on the injection tests. During shut-in the wellhead pressure fell from 8.7 to 4.4 MPa and still no seismicity was observed even though the hydraulic data from the previous tests indicated fracture opening had occurred.

4.1.5 Main cyclic soft stimulation treatment (11 to 13 August 2017)

Days 5–7 comprised the main cyclic soft stimulation treatment, with hydraulic and seismic results shown in Figs 10 and 11. First, a 24-hr long-term cycle was applied with 14 hr of medium-term cycles of 2 hr length followed by 10 hr of base rate injection at 2 l s⁻¹ (Fig. 10). The low rate during this cycling was half of the high rate to avoid fracture closure. The base rate was higher than before due to previous instabilities of the injection pump at 1 l s⁻¹. The injection rate was increased in steps of 2 l s⁻¹ up to 10 l s⁻¹ with the 10 l s⁻¹ cycle repeated four times. After this first CSS treatment the injected volume had increased to 859 m³ and the highest observed WHP was 20.1 MPa. During base rate injection the following night, WHP fell to 13.3 MPa, below the fracture opening pressure. Again, no seismic activity was registered.

Given that no seismic activity had been detected at this stage and to acquire data that could be used for hydraulic pulse test analysis (for which at least eight cycles are recommended) it was then decided to double the length of the next long-term cycle to 2 d, with cyclic injection continuing overnight (Fig. 11). Except for seven more repetitions of the same 10–5 l s⁻¹ cycle, the treatment schedule was the same as the previous day. The maximum WHP was 22.8 MPa and seismicity started to develop slowly with only eight individual events (all with $M_w < 0.5$) detected before the first traffic light alert.

4.1.6 Flow rate and pressure reduction due to orange traffic light alert (13 August 2017)

Just before the scheduled end, at 14:00 on 13 August, of the 10 l s⁻¹ high injection rate phase of the 13th repetition of the 10–5 l s⁻¹ cycling, a seismic event occurred at 13:58. The planned reduction in injection rate to 5 l s⁻¹ took place at 14:00, because by this time the earthquake had not yet been analysed. A preliminary magnitude of M_w 1.4 was reported by ~14:40. Since this earthquake thus appeared to be at the threshold of the orange alert level of the traffic light system (Fig. 5), the injection rate was decreased stepwise to 2 l s⁻¹ at 14:44 and to the lowest possible base rate of 1 l s⁻¹ ~1 hr later. After this adjustment was made, low-level microseismicity persisted, with 14 more events below M_w 1.0 until a M_w 1.9 event occurred the following day.

Subsequent re-analysis of the complete microseismicity data set gave M_w 1.2, rather than 1.4 for the event at 13:58 on 13 August; had this been reported at the time, it would have initiated a

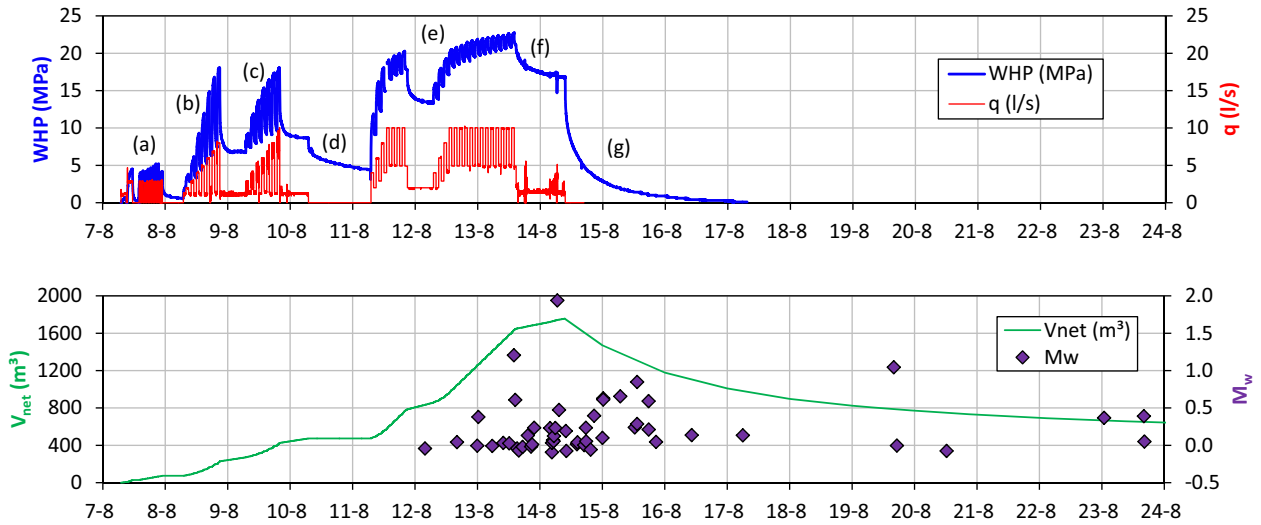


Figure 8. Overview of wellhead pressure (WHP), injection rate (q), injected net volume (V_{net}) and moment magnitude (M_w) of induced seismic events during the August 2017 CSS treatment in well PX-1. This treatment can be divided into seven phases: (a) initial injectivity determination, (b) fracture opening pressure determination, (c) hydraulic pulse tests, (d) shut-in, (e) main cyclic soft stimulation treatment, (f) pressure reduction due to orange traffic light alert and (g) complete flowback due to red traffic light alert. The magnitudes of the two events that triggered the alerts that led to actions under the TLS were determined in real time as M_w 1.4 (13 August 2017, 13:58) and M_w 1.8 (14 August 2017, 06:42). Their magnitudes were subsequently re-assessed, using the procedure described in detail, to M_w 1.2 and M_w 1.9, respectively.

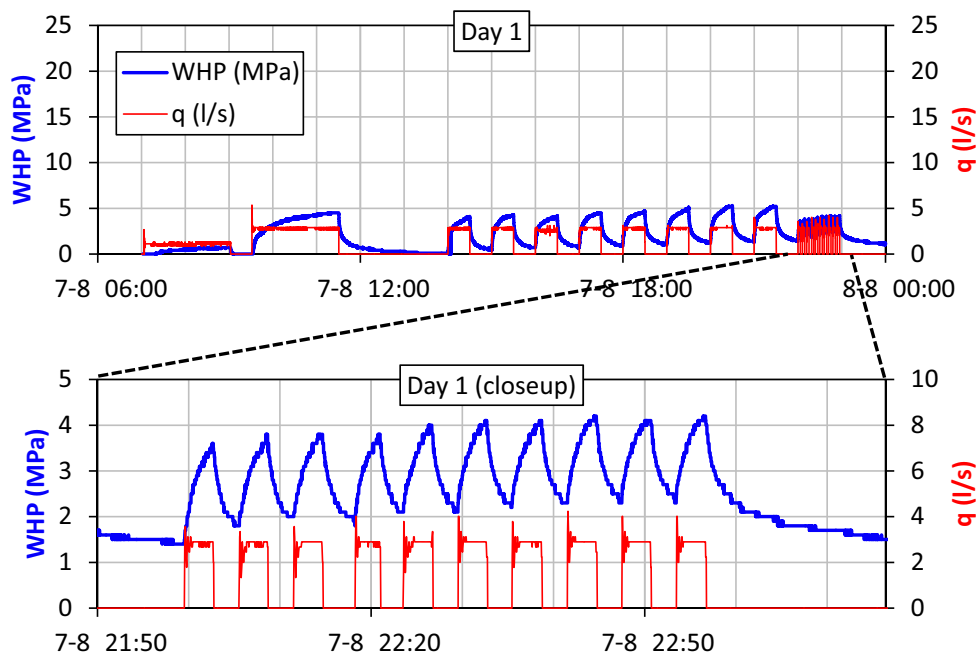


Figure 9. Wellhead pressure (WHP) and injection rate (q) during the first day of initial injection tests and close-up of short-term cycles during that day are shown. No seismicity was observed on that day.

yellow alert rather than an orange alert, and the response on site would have been different (*cf.* Fig. 5). The principal reason for this lower value, compared with the preliminary M_w 1.4, is that the preliminary analysis assumed a hypocentre at the bottomhole depth, ~ 4.2 km, whereas the revised analysis allowed hypocentral depth to vary and obtained a solution at ~ 3.8 km depth. The resulting shorter source–station distances to the various instruments mean less geometrical spreading and smaller corrections for anelastic attenuation, so the observed seismograms imply lower M_0 and M_w .

4.1.7 Complete flowback due to red traffic light alert (14 August 2017)

On Day 8, 14 August 2017, another significant seismic event occurred, at 06:42, for which M_w 1.9 is now reported. A preliminary estimate for this event of M_w 1.8 was determined, after a delay of almost 3 hr, initiating a red alert at 09:33. Injection was thus stopped immediately and well PX-1 was opened for flowback. The reanalysis revised the magnitude of this earthquake to 1.9; however, had this definitive magnitude been available in real time it would have made no difference to the implementation of the TLS (Fig. 5).

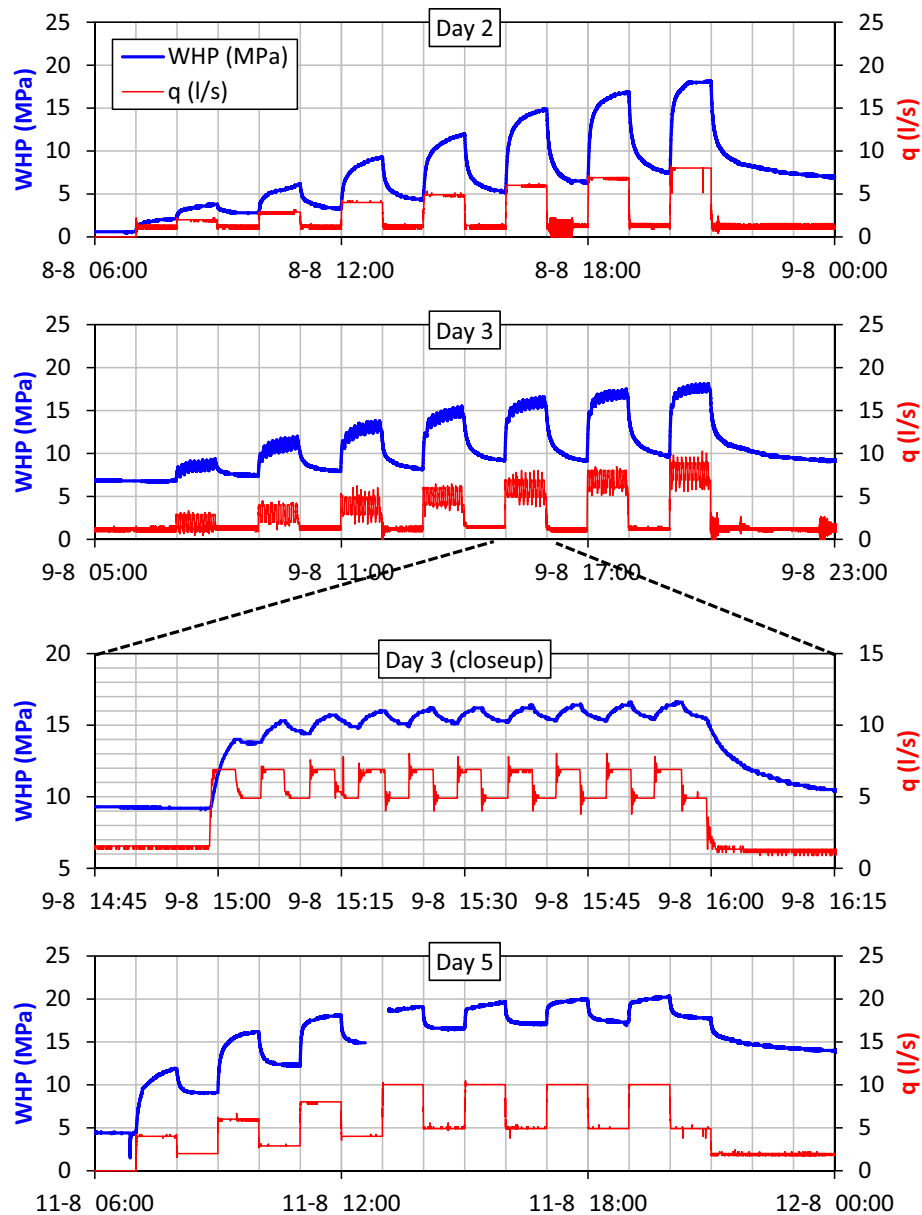


Figure 10. Wellhead pressure (WHP) and injection rate (q) during the 2 d of progressively increasing cyclic injection tests (Days 2 and 3), close-up of the pressure pulses on Day 3 and the first day of stimulation (Day 5). No seismicity was observed during the first 5 d.

Up to this point a total volume of 1756 m^3 had been injected (Fig. 11). The net volume, including the 1495 m^3 of water remaining from the previous PX-1 stimulation, was 3251 m^3 at this point. Flowback continued naturally until 22 August, producing a total volume of 1090 m^3 . During additional pumping and natural flowback until 5 September, in total 1771 m^3 was produced back. While seismicity continued to develop, during all this time, no additional earthquake of $M_w \geq 1.9$ occurred (Fig. 8), indicating that flowback may be a practical (easy to implement, but expensive, given the cost of treatment of the produced water) method to mitigate post-injection seismicity with larger magnitudes than the largest one observed during injection. Also, during and after the treatment no significant water level change was observed in well PX-2 that would indicate a hydraulic connection between the two wells.

As seen in Fig. 11, the flow rate and wellhead pressure increased again just before the 06:42 event occurred; this was due to malfunctioning of the injection pump. This pump had to be changed with the backup pump; this task took ~ 30 min, during which time well PX-1 was shut-in. It is interesting to note that these pressure fluctuations were within the critical range for fracture opening and closure (Figs 11 and 14). Whether or not the earthquake at 06:42 was influenced by short-term pressure changes in the stimulated fracture system due to this unintended flow rate increase and shut-in is unclear. A shear slip of a fracture caused the $M_w 1.4$ (later revised to $M_w 1.2$) event that triggered the orange traffic-light alert. Therefore, a slow pressure reduction was anticipated to avoid any larger slip events. The unintended pressure increase may have caused the same

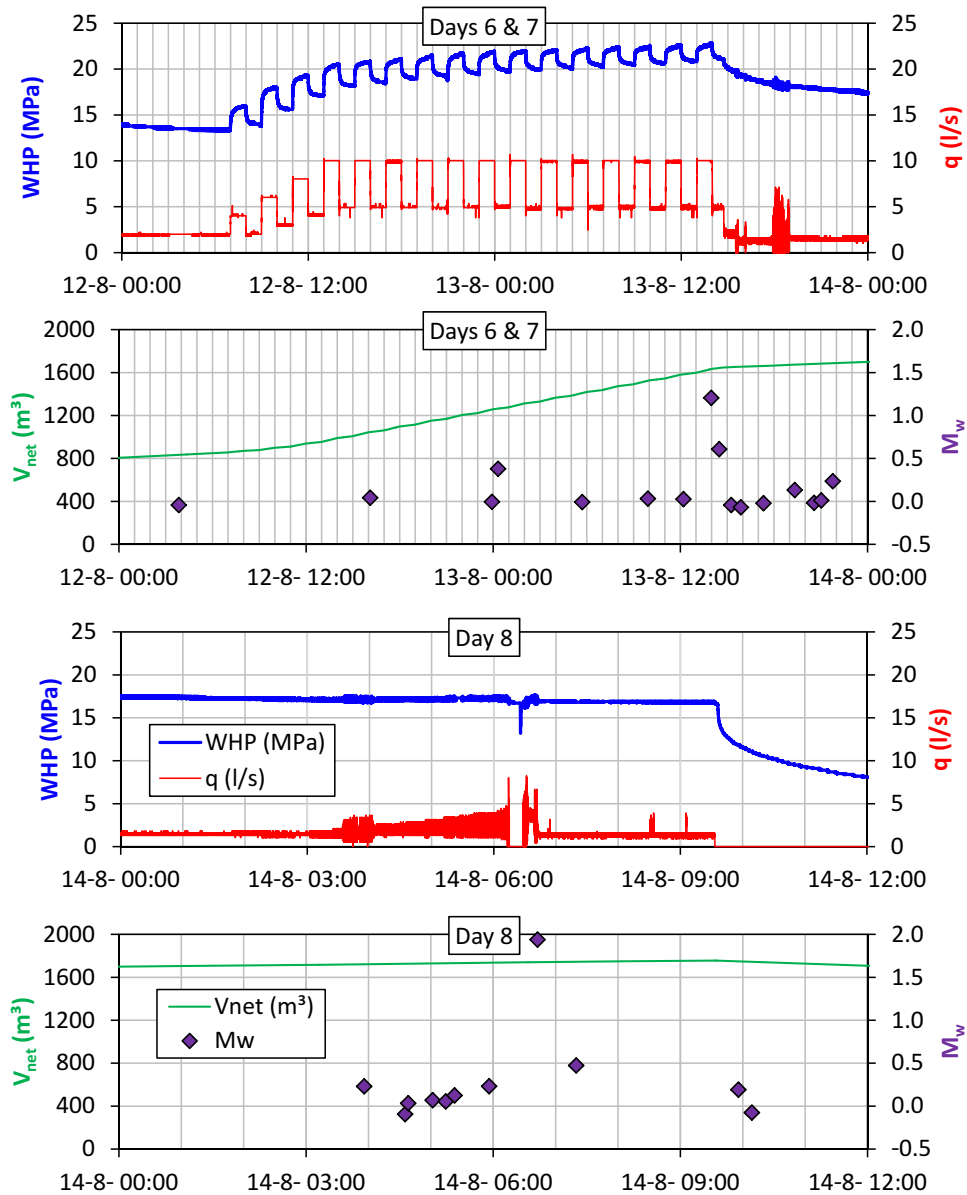


Figure 11. Wellhead pressure (WHP), injection rate (q), net volume (V_{net}) and moment magnitude (M_w) during the main stimulation treatment. After the M_w 1.2 event on Day 7 the flow rate was reduced to the minimum level and after the M_w 1.9 event on Day 8 flowback was initiated. The fluctuating flow rates and pressures were caused by a pump malfunction.

or a different fracture to slip and trigger the M_w 1.9 event. However, the event may as well have had no relation to these operations due to the random occurrence of seismic events and the delayed seismic response to injection. Thus, investigating this event in more detail may well lead to an improved understanding of earthquake triggering by fluid injection.

The 3-hr delay, between the earthquake at 06:42 on 14 August and the subsequent action being taken, resulted from a problem with the automated alerting system. The cause of this issue was identified, retrospectively, as an intermittent fault in the data connection between the recording system for the seismograph network and the server where data from station MSS01 was accessed to implement the TLS.

4.2 Characteristics of induced seismicity

Considering only the P - and S -phase onsets in the inversion problem presented in eq. (8), the vertical uncertainty of the hypocentre locations is smaller than the horizontal uncertainty. This is depicted by a hypocentre likelihood function presented in Fig. 12(a) for a single representative event. This difference in lateral and vertical location uncertainty is well-explained by the source–receiver geometry, as we mainly used P - and S -wave onset times that were exclusively picked on the borehole geophone array, at sensors with similar takeoff angle. This leads to good distance estimate in the radial direction, but poor azimuthal control (e.g. Bohnhoff & Zoback 2010; Bohnhoff *et al.* 2010; Kwiatak *et al.* 2010). The incorporation

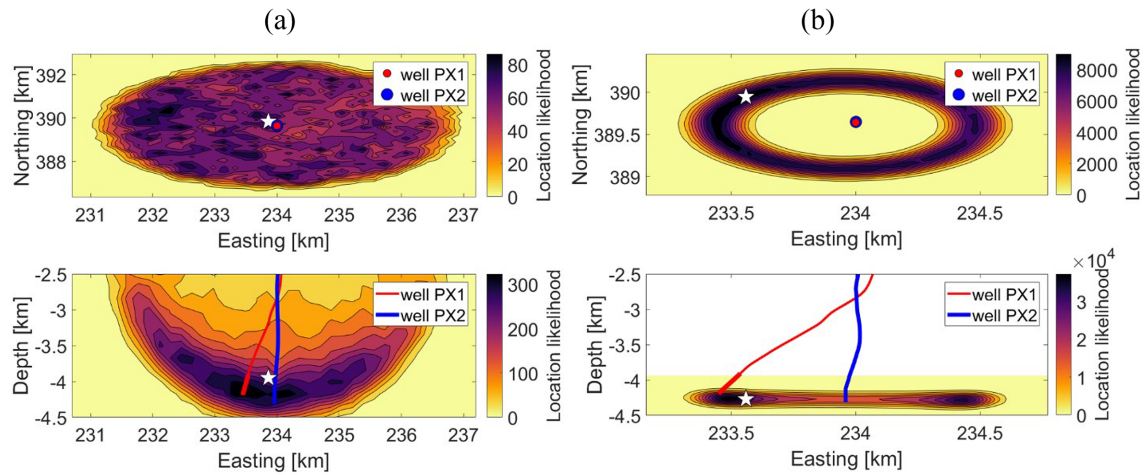


Figure 12. Examples of hypocentre location likelihood function for a selected representative event from 13 August 2017, as estimated using the Metropolis-Hastings Random Walk algorithm. Upper plots are plan views; lower plots are cross sections. (a) Location likelihood and preferred location using only P - and S -wave onsets. The white star shows the mode (most probable value) of the likelihood function. (b) Location likelihood and preferred location using P -, S -, PT - and ST -wave onsets. The white star represents the hypocentre location with minimum error.

of tube waves in the hypocentre inversion leads to improvement of location quality (Fig. 12b). This is expressed by toroidal likelihood function observed for all events for which the tube waves could be used in the inversion problem specified by eq. (8).

The likelihood functions for all earthquakes with tube waves identified present common features. The vertical and horizontal uncertainties are ~ 125 and ~ 600 m, respectively. The maximum of the likelihood function (= hypocentre location), ~ 500 m away from open-hole section of PX-2, is located either WNW of well PX-2, in close proximity to the open-hole section of injection well PX-1, or at the same distance in the opposite direction. Overall, this leads to events clustering in two clouds on opposite sides of well PX-2 (Fig. 13). The few events located between these clouds, close to well PX-2, were located without PT and ST phases, and thus less well constrained (*cf.* Fig. 12a).

This clustering of events, rather than the expected toroidal distribution, is caused by the slight inclination of well PX-2 along the geophone array (Fig. 4), which enabled the analysis procedure to resolve the azimuth of the incoming seismic waves. However, given the near symmetry of the sensor configuration, we cannot resolve whether the occurrence of the events in two separate clusters is indeed real by using only P -, S -, PT - and ST - phase onsets. To solve this ambiguity, we applied the polarization analysis (e.g. Jurkevics 1988). For that purpose, we rotated the three-component seismogram into the LQT coordinate system and identified the direction of incoming P -wave (azimuth, incidence angle). For 10 events of the SE cluster with suitable signal-to-noise ratio, the polarization analysis reported incidence angles ranging between 5° and 20° and azimuth angles between 260° and 360° . For the two largest events, which were previously located within in the SE cluster, we obtained incidence angles between 5° and 15° and azimuth angles between 300° and 350° which clearly corresponds to the WNW cluster. This means that the SE cluster is indeed an artefact of the hypocentre inversion problem. In consequence, it is very likely that all events, including those for which the polarization analysis could not be performed, occurred in close proximity to the open-hole section of injection well PX-1.

4.3 Data analysis

4.3.1 Analysis of injectivity development

To facilitate discussion, the aforementioned dynamic wellhead injectivity index (DWII) parameter will from now on be referred to as injectivity. The development of injectivity at the end of each high injection rate phase is shown in Fig. 14; measured values range between ~ 0.2 and ~ 0.8 $\text{l s}^{-1} \text{MPa}^{-1}$. Overall these injectivities are more than an order of magnitude lower than would be necessary for economic operations, for which ~ 10 $\text{l s}^{-1} \text{MPa}^{-1}$ would be needed (e.g. Baria *et al.* 1999). The first test yielded an injectivity of 2.8 $\text{l s}^{-1} \text{MPa}^{-1}$ at WHPs of < 1 MPa and is not included in the figure; it is indicative of a small volume of permeable rock near the borehole. In the subsequent tests on the same day the injectivity decreased to almost 0.3 $\text{l s}^{-1} \text{MPa}^{-1}$ due to the increase of injected volume that could not flow away from the borehole at pressures of less than ~ 5 MPa. With progressively increasing flow rates on Day 2 it can be seen that the injectivity decreased from 0.55 to 0.40 $\text{l s}^{-1} \text{MPa}^{-1}$ due to the increased injected volume. However, during the last two cycles, the injectivity increased, presumably because of fractures opening due to the elevated pressures, leading to a lower rate of pressure increase with increasing injection rate. Interestingly, on the third day, when pressure pulses were applied, the injectivity increased continuously from a much lower level (0.21 $\text{l s}^{-1} \text{MPa}^{-1}$) to approximately the same level as the previous day (> 0.4 $\text{l s}^{-1} \text{MPa}^{-1}$). During the different phases of the main stimulation treatment injectivity evolution was comparable. Injectivity increased with increasing flow rate (and thus pressure) until the maximum was reached during the first 10 l s^{-1} cycle. During subsequent cycles the flow rates were the same, but the pressure increased slightly due to the increased injected net volume. Therefore, the injectivity decreased continuously from this point on.

The WHP-injection rate plot in Fig. 14(a) was used to determine the fracture opening pressure. In this plot a significant change of gradient can be observed between 15 and 17 MPa on Day 2 (no pressure pulses) and between 14 and 16 MPa on Day 3 (with

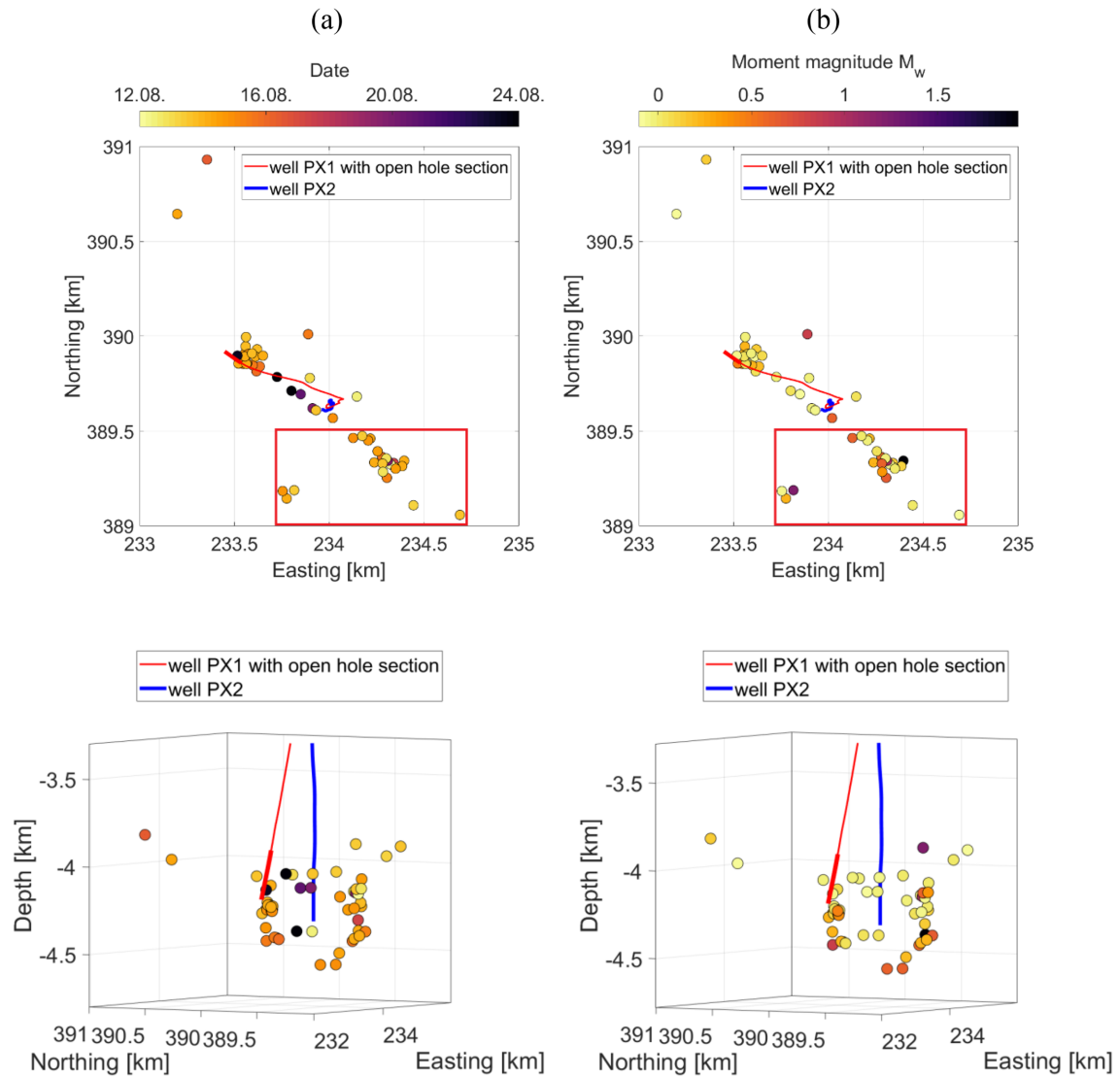


Figure 13. Plan views and 3-D views of the locations of the 52 seismic events detected during the stimulation, colour coded (a) with time and (b) with moment magnitude. Note that the SE cluster marked by the rectangle is likely to be an artefact as indicated by polarization analysis.

pressure pulses). This indicates a slightly lower or similar fracture opening pressure when using pulsed treatments. According to Park *et al.* (2017b) this fracture opening pressure is indicative of hydroshearing. While the pressures increase each day due to the increasing cumulative injected fluid volume, after each day the slopes of the trend lines seem to decrease, indicating improving hydraulic performance.

Fig. 14(b) shows the variation of dynamic differential wellhead injectivity index (DDWII), designated as differential injectivity from now on. This parameter is more indicative of changes in injectivity than absolute injectivity. In all tests the differential injectivity was $\sim 0.5 \text{ l s}^{-1} \text{ MPa}^{-1}$ up to 15 MPa WHP. Above 15 MPa it increased, reaching $\sim 2.7 \text{ l s}^{-1} \text{ MPa}^{-1}$ at the highest pressures. This plot shows the pressure-dependent injectivity of the system and the abrupt injectivity increase after fracture opening, which were similar in all performed tests. Fig. 14(c) illustrates the variations in DWII over time, demonstrating that this parameter reverts to low values at the start of each injection phase, indicating that the increases observed at higher pressures are not permanent effects.

4.3.2 Conventional well testing analysis

Wellhead pressure development of three shut-in periods (after injection at 3 l s^{-1} for 2 hr on Day 1, after the last injection on Day 1, and during Day 4) and the final flowback after the stimulation were analysed using classical well test analysis. Fig. 15 shows the pressure fall-off and derivative curves in a log-log plot and the associated matches to obtain the hydraulic parameters given in Table 1. For this analysis, the reservoir height has been set to 291 m, and a fluid viscosity of 0.3 mPa s , a compressibility of $4.5 \times 10^{-10} \text{ Pa}^{-1}$, a porosity of 1 per cent, and a well radius of 0.108 m were used. Sensitivity analyses revealed a significant misfit for all analysed pressure curves if the parameters skin, transmissivity and distance to the no-flow boundary are reduced or increased by 10 per cent. Hence, the uncertainties and the associated error bounds are less than ± 10 per cent. The data from the shut-in phases do not indicate a no-flow boundary. Regarding the flowback, the best pressure match is achieved by including a no-flow boundary at a distance of $\sim 91 \text{ m}$. This no-flow boundary may be interpreted as an impermeable fault or the boundary of the activated volume due to the stimulation in

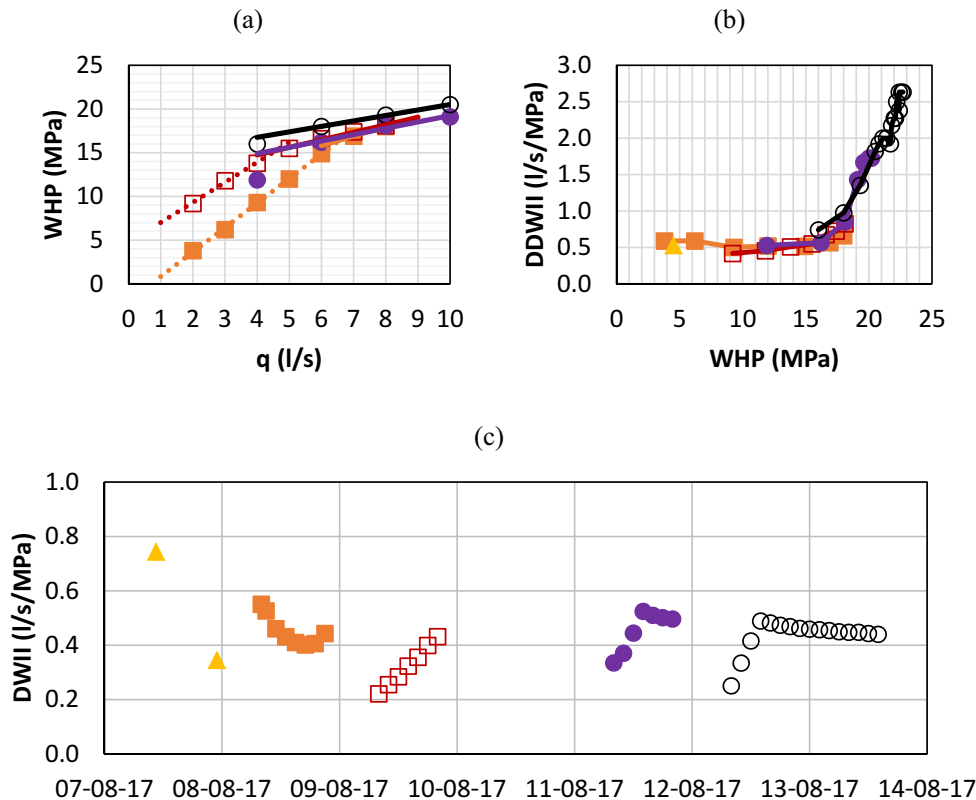


Figure 14. Illustrations of changes in injectivity of Well PX-1 during the August 2017 injection experiment colour coded by injection phase. (a) Graph of wellhead pressure (WHP) against injection rate. From the change in gradient, the fracture opening pressure was determined to lie between 15 and 17 MPa. (b) Graph of dynamic differential wellhead injectivity index (DDWII or differential injectivity) against WHP. Up to 15 MPa the DDWII is approximately constant at $\sim 0.5 \text{ l s}^{-1} \text{ MPa}^{-1}$. Above this level the hydraulic behaviour changes to a more permeable system, interpreted as fracture opening. (c) Dynamic wellhead injectivity index (DWII) variations over time.

an almost impermeable rock. The hydraulic parameters from this analysis can be regarded as valid for low pressures and a closed fracture system.

The transmissivity kh decreases from 1.15×10^{-13} to $3.44 \times 10^{-14} \text{ m}^3$, whereas the skin s decreases to more negative values, from -2.40 to -5.76 , hence indicating improved hydraulic access between the well and the reservoir. The productivity index depends on transmissivity as well as on skin. Calculated according to the Lee (1982) pseudo steady-state solution, the productivity index shows a slight decrease from 0.44 to $0.34 \text{ l s}^{-1} \text{ MPa}^{-1}$. Similar values are obtained by applying the solution for a well doublet with a 600 m distance between injection and production well (see Table 1). This slight decrease in productivity index is accompanied by an increase in initial WHP from -0.36 MPa (water level in well PX-1 below surface at the beginning of the treatment) to 3.3 MPa during the last two tests. The slightly decreasing injectivity index and the initial pressure increase can be interpreted as indicating a limited isolated reservoir volume where fluid injection was impeded by the total injected volume.

4.3.3 Harmonic pulse testing analysis

A detailed description of the interpretation of harmonic pulse testing, including derivation of the underlying theory, is given by Fokker *et al.* (2018a). The results obtained by Fokker *et al.* (2018a) have been updated by changing the fluid, reservoir and well properties

to the ones used in the conventional well testing analysis presented above. This allows a direct comparison of both analyses.

The harmonic pulse tests during Days 1–3 and during the main stimulation treatment (Days 5–7) have been analysed using SPP data. For the tests with longer cycle times, many more frequencies have pressure amplitudes that exceed the background level. Also, the fundamental frequency (i.e. the smallest frequency present in the spectrum) is much lower—this corresponds to a larger investigation area around the well. Acceptable fits between observations and theory are obtained with the parameters listed in Table 1. During the test on Day 3, the pulse testing during cycles of increasing injection rate allowed the effect of pressurization to be monitored. The responses to these cycles, indicated in Fig. 16, show only a small effect. However, it must be noted that the cycle time of these tests is so short that a large part of the response at even the lowest frequencies is controlled by the wellbore storage. Overall, the transmissivity and productivity determined from these pulse tests during the first 3 d is similar to those obtained from conventional well test analysis (fall off #1 and #2 during Day 1). Thus, the initial productivity is reasonably well constrained between 0.41 and $0.52 \text{ l s}^{-1} \text{ MPa}^{-1}$ (Table 1), similar to the differential injectivity before fracture opening, determined as $\sim 0.5 \text{ l s}^{-1} \text{ MPa}^{-1}$ (Fig. 14).

The last two stages of the operation sequence (Day 5 and Days 6–7) employed alternating high- and low-rate injection pulses of 1 hr each. For both these tests, many frequency components with magnitude peaks could be identified, even for the tests on Day 5. The small number of only four cycles apparently did not seriously harm the effectiveness of this test. The response observed in the

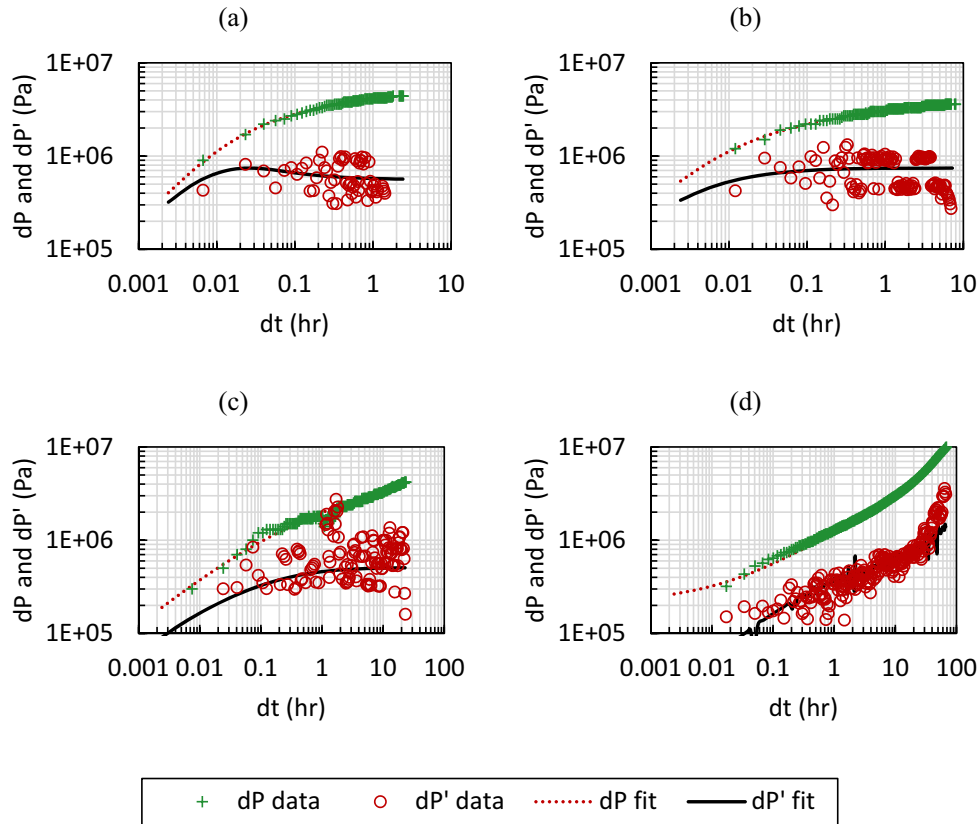


Figure 15. Log–log plots of conventional well testing analysis with pressure (dP) and pressure derivative (dP') curves over time since start of shut-in or start of flowback. Data points indicate field data; lines show fitted model results. (a) Day 1#1 after 2 hr of injection at 3 l s^{-1} , (b) Day 1#2 after last injection of that day, (c) Day 4 after 3 d of injection tests and Day 8 after the end of all injections.

Table 1. Results of hydraulic analysis.

	Fall off #1 Day 1	Fall off #2 Day 1	Pulse test Day 1–3	Fall off Day 4	Pulse test Day 5	Pulse test Day 6–7	Flowback Day 8
Cumulative net volume V_{net} (m^3)	28	47	28–473	473	571–785	955–1647	1756–897
Initial pressure p_0 (MPa)	-0.36	0.21	-	3.34	-	-	3.30
Transmissivity kh (10^{-13} m^3)	1.15	0.93	1.97	0.52	5.92	7.90	0.34
Permeability k (10^{-15} m^2)	0.40	0.32	0.68	0.18	2.03	2.71	0.12
Skin s (-)	-2.40	-3.08	0.00	-3.99	0.00	0.00	-5.76
PI (l/s/MPa) pseudo steady-state $R = 600 \text{ m}$	0.44	0.41	0.52	0.28	1.57	2.10	0.34
PI (l/s/MPa) well doublet $d = 600 \text{ m}$	0.39	0.35	0.48	0.24	1.44	1.92	0.25
Distance to no-flow boundary L (m)	-	-	-	-	-	-	90.7
Storage coefficient C ($\text{m}^3 \text{ Pa}^{-1}$)	$4.12\text{E-}08$	$1.71\text{E-}08$	$5.60\text{E-}09$	$2.59\text{E-}09$	$7.47\text{E-}09$	$7.47\text{E-}09$	$2.50\text{E-}09$

Results are shown for three fall-off periods and one flowback using conventional well test analysis (after injection) and three periods of pulse injection interpreted by harmonic pulse testing analysis (during injection).

last tests points to an increased transmissivity up to $\sim 6\text{--}8 \times 10^{-13} \text{ m}^3$, presumably due to opening fractures. Due to fracture opening, the PI thus increased by a factor of ~ 4 to $2.1 \text{ l s}^{-1} \text{ MPa}^{-1}$. However, this increase was only observed at elevated pressures ($> 15 \text{ MPa}$ WHP) and was not maintained when the pressure was subsequently reduced.

4.3.4 Analysis of seismological data

The seismological data set allows us to draw some significant conclusions. First, the seismicity started relatively late during the treatment. The time between the onset of the first injection and the first seismic event detected in real-time was $\sim 5 \text{ d}$; the time between overcoming the critical pressure for fracture opening and the first

seismic event was $\sim 3.5 \text{ d}$. The lack of seismicity at the start may be attributed to the ‘Kaiser-effect’, meaning the absence of seismicity during loading, if the prior maximum load level is not exceeded (Baisch *et al.* 2002; Zang *et al.* 2014). This is because well PX-1 was previously stimulated (in December 2016) with a larger water volume and at higher pressures for a longer time.

Second, a clear correlation between the injected net volume and the maximum magnitude of the events was observed (Fig. 17). After the M_w 1.9 event, the injected net volume was reduced by flowback. During this time, seismic event magnitudes were lower than the largest magnitude observed during injection ($M_w < 1.9$). This observation supports the hypothesis that controlling and limiting the injected net volume is a key element and an easy to use tool to eventually avoid larger magnitude events during and shortly after

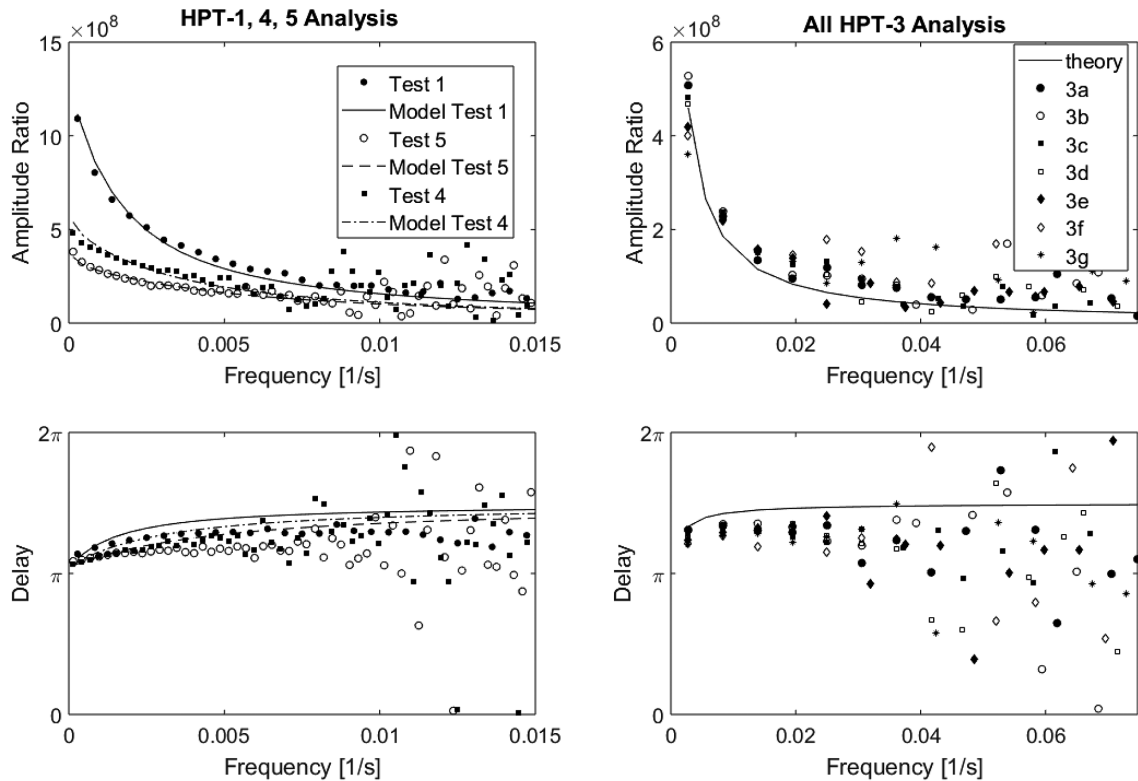


Figure 16. Analysis of all harmonic pulse test monitoring spectra for Days 1 (HPT-1), 3 (HPT-3), 5 (HPT-4) and 6–7 (HPT-5) from Fokker *et al.* (2018a). Parameters derived from matching the model responses are listed in Table 1.

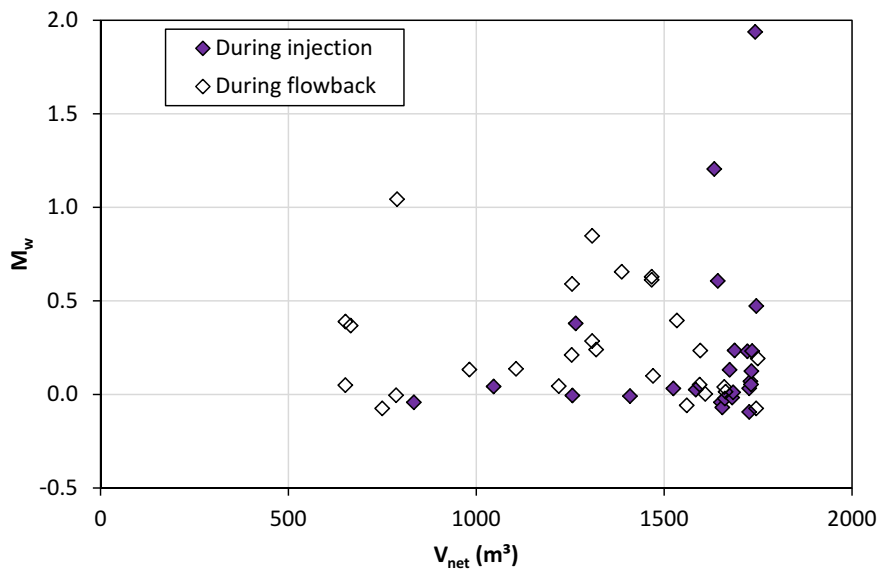


Figure 17. Relation between net volume (V_{net}) injected into well PX-1 in August 2017 and moment magnitude (M_w) of induced seismic events.

the treatment. During injection, the logarithm of cumulative seismic moment increased with the injected volume. In contrast, only minor seismic moment was released during the subsequent flowback (Fig. 18).

5 DISCUSSION

This study describes the first cyclic soft stimulation treatment performed at an EGS reservoir; lessons can thus be learned. During

the CSS treatment in Pohang, the injection rate was changed >250 times. Nevertheless, the stimulation depended on pumps being operated manually to an agreed schedule; especially for pulse tests, automated control would be preferable. Also, since stable operation of the injection pump is critical to project success, we recommend that any future project is designed with two pumps connected in parallel, each rated so it can individually handle the full range of flow rates required. Then, if either pump fails, the other one can handle the injection without interruption. Finally, an optimized seismic network

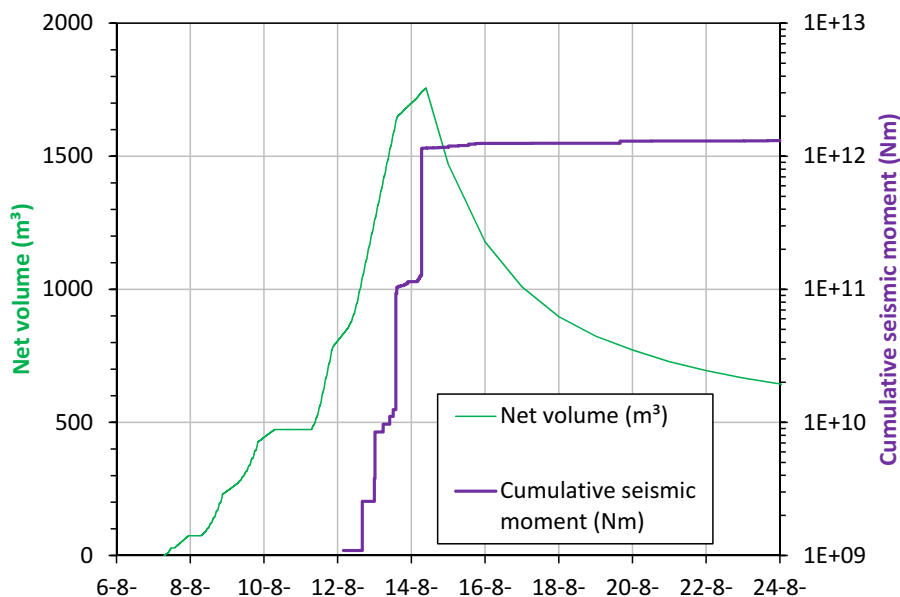


Figure 18. Temporal evolution of the cumulative seismic moment (M_0) and net volume (V_{net}) injected in August 2017.

design considering specific needs of network geometry (Bohnhoff *et al.* 2018) and applying *in situ* noise conditions and medium attenuation characteristics (Kwiatak & Ben-Zion 2016) would provide better hypocentral locations for smaller events. At Pohang the pervasive outcrop of Middle Miocene mudstone (Fig. 1) made surface seismometer stations (Fig. 4) problematic; the high attenuation of seismic waves in this relatively thin layer led to low SNR, limiting the data produced by these stations. Placement of stations in shallow boreholes, reaching the underlying Early Miocene tuff, would have been preferable; the evidence from station MSS01, located within outcrop of this tuff, indicates better SNR characteristics.

Before the CSS treatment in August 2017, a conventional hydraulic stimulation was performed in well PX-1 in December 2016. During this first PX-1 stimulation 3907 m³ water was injected with a maximum flow rate of 18 l s⁻¹ and a maximum WHP of 27.7 MPa. The largest portion was injected continuously at a constant flow rate of 10 l s⁻¹ over ~3 d. In total, 835 seismic events were detected during the stimulation with a maximum local magnitude of 2.3 and with the largest magnitudes occurring during shut-in phases. ‘Injectivity’ (DDWII) increased to ~3.1 l s⁻¹ MPa⁻¹ above 15–17 MPa WHP (Kim *et al.* 2017a; Park *et al.* 2017b). Until the start of the CSS treatment in August 2017, 2412 m³ of water were produced back, meaning that 1495 m³ of injected water remained in the subsurface. During the CSS treatment in August 2017, 1756 m³ of the same water was injected in the same well with a maximum flow rate of 10 l s⁻¹ and a maximum WHP of 22.8 MPa. Together with the remaining previously injected volume, the largest cumulative net injection volume during the CSS treatment was 3251 m³. The injection scheme was cyclic injection with progressively increasing flow rates instead of continuous injection at constant flow rate. 52 induced seismic events were detected in real-time with a maximum moment magnitude of 1.9 during injection and seismic magnitudes did not increase during flowback. A significant injectivity increase was observed at the same WHP range between ~15 and 17 MPa with the DDWII increasing from a base level of ~0.5 l s⁻¹ MPa⁻¹ to a maximum of ~2.6 l s⁻¹ MPa⁻¹. After the CSS treatment 1771 m³ water were produced back, leading to a lower net injection volume as before. No comparison can be made about the sustainable long-term

injectivity increase. In summary, less water was injected, at lower flow rates and lower pressures, followed by a complete flowback of the injected water without shut-in during the August 2017 stimulation compared to the December 2016 stimulation. This led to less induced seismic events, lower magnitude seismic events, and a lower maximum DDWII during the August 2017 stimulation compared to the December 2016 stimulation. Based on this limited information, and due to the different purposes of the treatments, it cannot be judged whether one of the stimulation designs is more successful than the other in terms of seismicity control or injectivity increase. However, the primary constraint for the CSS treatment, no induced seismicity with $M_w \geq 2.0$ during either the injection or subsequent flowback phase, was satisfied. We anticipate a comprehensive comparison between the CSS concept applied in August 2017 and the conventional monotonic injection from December 2016 in PX-1 after the data from the previous stimulation has been re-assessed and published. This is a challenging task, because both treatments were performed sequentially in the same openhole section with a significant time gap of more than half a year, the neighboring borehole PX-2 was stimulated three times in the same time period, and the seismic monitoring system setup was different. To properly compare different injection schemes, multiple stimulations in separate stages in the same formation along a horizontal borehole would be necessary. This could be done analogously to previous mine-scale experiments (e.g. Zang *et al.* 2017a). An alternative would be to repeatedly alternate the same continuous and cyclic injection schemes during a stimulation campaign.

As stated earlier, the maximum magnitude observed during this cyclic soft stimulation treatment was below the target threshold of M_w 2.0. Even though the maximum magnitude of induced seismicity may have been higher than M_w 1.9, given the random nature of earthquakes, this observation indicates that the concept may be a promising path to follow as potential seismic risk mitigation measure. This was the result of integrating prior reservoir knowledge into the cyclic soft stimulation design, consisting of long-, medium- and short-term cycles, as well as a slow and stepwise pressure increase and decrease, no shut-in but flowback with sufficient storage capacity on site, low pressures, limited maximum net

volume and a traffic light system for cyclic injection. Analysis of the influence and significance of each of these factors is underway. Pending this analysis, we consider that limiting the injection volume and immediate flowback were two key elements of the CSS concept that limited the maximum magnitude of the induced seismic events. Further field tests will be needed to refine this concept and improve understanding of the underlying processes. This requires investigations into the fundamental geomechanical processes of induced seismicity (Gaucher *et al.* 2015). Most importantly, it remains to be demonstrated that this stimulation concept can cause a significant permanent increase in the hydraulic performance of a reservoir.

Given the limited injectivity increase observed at Pohang, it is recommended to apply this concept with a significantly larger fluid volume over a much longer time. Typical injection volumes needed for sufficient injectivity enhancement are at least an order-of-magnitude higher than those used in this test stimulation (*cf.* Baria *et al.* 1999). The injected volume would have to be partitioned in multiple steps so that the maximum injected net volume does not exceed the site-specific critical volume in each step. This critical total net volume was estimated to be $\sim 3600 \text{ m}^3$ for the PX-1 well in Pohang based on a local net volume—seismic magnitude relation. Such partitioning of the injected fluid volume might be achieved in two different ways. The first option would be to produce the injected water back to the surface, filter or treat it, and then re-inject it back into the reservoir. This process would need to be repeated until the desired injectivity is reached. In this case, the injectivity increase would depend on the anticipated hydraulic fatiguing effect and development of new fractures due to stress re-distributions resulting from previous injections. Otherwise, injectivity increase may rely on stimulation of rock volumes that have not been stimulated previously, as indicated by the Kaiser effect. The second option would be to inject the fluid into multiple stages along the wellbore. The critical volume would here be injected in each of the separate stages. The stages should not be hydraulically connected to each other to be able to seal off potential stages that may act as dominant fluid pathways and lead to early thermal breakthrough at the production well. Also they should not be connected to a major subsurface structure that may bear the potential for larger seismic events to be triggered by the fluid injection. Since the site conditions did not indicate sufficient permanent hydraulic performance increase by the stimulation treatments and no hydraulic connection between the two wells was established, it was recommended to fully analyse the acquired data and plan the next steps (e.g. a possible side-track of well PX-2) accordingly.

However, after a M_w 5.5 earthquake occurred near the site on 15 November 2017 (KMA 2018), the Pohang EGS project was suspended. Potential causal links between EGS site operations and this M_w 5.5 event are currently under investigation by different research groups and a governmental commission using a variety of subsets of data (e.g. Dahm *et al.* 2018; Grigoli *et al.* 2018; Kim *et al.* 2018a). These studies intend to answer the question whether and how a causal relation between EGS site activities and the M_w 5.5 event can be established or excluded. Related to this, it is also investigated whether or not a causal relation between the CSS treatment presented in this manuscript and this anomalously large magnitude event from 15 November 2017 can be established or excluded. Answering these questions requires a detailed analysis of many parameters such as structural geology, stress field and hydrogeology. Since these analyses are ongoing, an answer to these questions cannot be provided here.

6 CONCLUSIONS

The first field application of the cyclic soft stimulation concept at the Pohang EGS site in Korea in August 2017 has been described and analysed and the technical feasibility of the concept has been established. This CSS involved injection of 1756 m^3 of surface water during 8 d into well PX-1 with a maximum flow rate of 10 l s^{-1} and a maximum wellhead pressure of 22.8 MPa. The deployment of a downhole seismometer array was essential to study the resulting induced seismic events, most of which were too small to be detected by surface seismometers. The provision of real-time earthquake location and magnitude determination at the site contributed to successful implementation of the traffic light system for responding to seismicity. Thus, following a M_w 1.2 event, pressure and flow rate were reduced. Following a subsequent M_w 1.9 event, flowback was initiated, during which no larger-magnitude events occurred. This M_w 1.9 event was below the anticipated target magnitude of M_w 2.0.

The analysis indicates a pressure-dependent hydraulic performance increase up to productivities of $2.1 \text{ l s}^{-1} \text{ MPa}^{-1}$, a decreased well skin and fracture opening at elevated wellhead pressures of 15–17 MPa, but there was no significant permanent productivity increase above $0.5 \text{ l s}^{-1} \text{ MPa}^{-1}$. Further field tests are needed to validate and refine this stimulation concept. In particular, longer field experiments with larger volumes, partitioned into multiple stages, are required to establish whether hydraulic performance can be significantly and sustainably increased by cyclic soft stimulation, while still reducing the magnitude of the largest induced seismic events.

These experiments cannot be performed at the Pohang site as this EGS project is currently suspended because of a M_w 5.5 earthquake that occurred nearby in November 2017. Possible causal connections between EGS site activities and this event are currently being investigated.

ACKNOWLEDGEMENTS

The authors are grateful for the funding received from the European Commission Horizon 2020 research and innovation programme under grant agreement No. 691728 (DESTRESS). This work was also supported by the New and Renewable Energy Technology Development Program of the Korea Institute of Energy Technology Evaluation and Planning (KETEP) through a grant (No. 20123010110010) funded by the Korean Government's Ministry of Trade, Industry & Energy and by the Korea-EU Joint Research Support Program of the National Research Foundation of Korea (NRF) through a grant (No. NRF-2015K1A3A7A03074226) funded by the Korean Government's Ministry of Science and ICT. We also thank the participating staff and students from all the partner institutions involved in the field operations. We are also grateful to the reviewers for their thoughtful and constructive comments.

REFERENCES

- Abercrombie, R.E., 1995. Earthquake source scaling relationships from -1 to 5 ML using seismograms recorded at 2.5 km depth, *J. geophys. Res.*, **100**(B12), 24 015–24 036.
- Andrews, D.J., 1986. Objective determination of source parameters and similarity of earthquakes of different size, editors: Das S., Boatwright J., Scholz, C.H., in *Earthquakes Source Mechanics*, **37**, American Geophysical Union.
- Baisch, S., Bohnhoff, M., Ceranna, L., Tu, Y. & Harjes, H.P., 2002. Probing the crust down to 9 km depth: a unique long-term fluid injection experiment at the KTB superdeep drilling hole, Germany, *Bull. seism. Soc. Am.*, **92**(6), 2369–2380.

- Baisch, S., Voeroes, R., Rothert, R., Stang, H., Jung, R. & Schellschmidt, R., 2010. A numerical model for fluid injection induced seismicity at Soultz-sous-Forêts, *Int. J. Rock Mech. Min.*, **47**(3), 405–413.
- Baria, R., Baumgärtner, J., Rummel, F., Pine, R.J. & Sato, Y., 1999. HDR/HWR reservoirs: concepts, understanding and creation, *Geothermics*, **28**(4-5), 533–552.
- Boatwright, J., 1978. Detailed spectral analysis of two small New York State earthquakes, *Bull. seism. Soc. Am.*, **68**(4), 1117–1131.
- Bohnhoff, M., Malin, P.E., ter Heege, J., Leflandre, J.-P. & Sicking, C., 2018. Suggested best practice for seismic monitoring and characterization of non-conventional reservoirs, *First Break*, **36**(2), 59–64.
- Bohnhoff, M. & Zoback, M.D., 2010. Oscillation of fluid-filled cracks triggered by degassing CO₂ during leakage from its storage reservoir, *J. geophys. Res.*, **115**, B11305, doi:10.1029/2010JB000848.
- Bohnhoff, M., Zoback, M.D., Chiaramonte, L., Gerst, J. & Gupta, N., 2010. Seismic detection of CO₂ leakage along monitoring wellbores, *Int. J. Greenhouse Gas Con.*, **4**(4), 687–697.
- Boore, D.M. & Boatwright, J., 1984. Average body-wave correction coefficients, *Bull. seism. Soc. Am.*, **74**, 1615–1621.
- Bormann, P. & Di Giacomo, D., 2011. The moment magnitude Mw and the energy magnitude Me: common roots and differences, *J. Seismol.*, **15**(2), 411–427.
- Brehme, M., Blöcher, G., Regenspurg, S., Milsch, H., Petrauskas, S., Valickas, R., Wolfgramm, M. & Huenges, E., 2017. Approach to develop a soft stimulation concept to overcome formation damage – a case study t Klaipeda, Lithuania, in *Proceedings of the 42nd Workshop on Geothermal Reservoir Engineering*, Stanford, CA, USA, 13–25 February, SGP-TR-212.
- Bromley, C.J., 2014. Seismicity and subsidence: examples of observed geothermal deformation synergies from New Zealand, in *Proceedings of the 39th Workshop on Geothermal Reservoir Engineering*, Stanford, CA, USA, 24–26 February, SGP-TR-202.
- Cerfontaine, B. & Collin, F., 2017. Cyclic and fatigue Behaviour of rock materials: review, interpretation and research perspectives, *Rock Mech. Rock Eng.*, **51**(2), 391–414.
- Choi, P.Y., 2006. ‘Singwang strike-slip duplex’ around the Pohang Basin, SE Korea: its structural evolution and role in opening and fill of the Miocene basin, *Geosci. J.*, **10**(2), 145–157.
- Chough, S.K., Kwon, S.-T., Ree, J.-H. & Choi, D.K., 2000. Tectonic and sedimentary evolution of the Korean peninsula: a review and new view, *Earth-Sci. Rev.*, **52**(1-3), 175–235.
- Chough, S.K. & Sohn, Y.K., 2010. Tectonic and sedimentary evolution of a Cretaceous continental arc-backarc system in the Korean peninsula: New view, *Earth-Sci. Rev.*, **101**(3-4), 225–249.
- Dahm, T., Hainzl, S., Hofmann, H., Cesca, S., Zimmermann, G. & Huenges, E., 2018. Was the Mw 5.5, November 15, 2017, Pohang, South Korea, Earthquake related to anthropogenic activities: a physics-based study on trigger probabilities, in *Proceedings of the European Seismological Commission 36th General Assembly*, Valetta, Malta, 2–7 September 2018, ESC2018-S32-676.
- Deichmann, N. & Giardini, D., 2009. Earthquakes induced by the stimulation of an enhanced geothermal system below Basel (Switzerland), *Seismol. Res. Lett.*, **80**(5), 784–798.
- Diaz, M., Jung, S.G., Zhuang, L. & Kim, K.Y., 2018. Comparison of acoustic emission activity in conventional and cyclic hydraulic fracturing in cubic granite samples under tri-axial stress state, in *Proceedings of the 52nd US Rock Mechanics / Geomechanics Symposium*, Seattle, WA, USA, 17–20 June, ARMA 18–1160.
- Diaz, M.B., Jung, S., Zhuang, L., Kim, K.Y., Shin, H.-S. & Min, K.-B., 2017. Quantitative comparison of hydraulically induced fractures under continuous and cyclic injection on Pocheon granite, in *Proceedings of the 19th International Conference on Soil Mechanics and Geotechnical Engineering*, pp. 3435–3438, Seoul, Korea, September 17–21.
- Di Bona, M. & Rovelli, A., 1988. Effects of the bandwidth limitation on stress drops estimated from integrals of the ground motion, *Bull. seism. Soc. Am.*, **78**(5), 1818–1825.
- Economides, M.J. & Nolte, K.G., 2000. *Reservoir Stimulation*, 3rd ed., Wiley.
- Farkas, M., Hofmann, H., Zimmermann, G., Zang, A. & Yoon, J.S., 2018. Numerical investigation of cyclic hydraulic stimulation and related induced seismicity in Pohang fractured geothermal reservoir, in *Proceedings of the 2nd International Discrete Fracture Network Engineering Conference*, Seattle, WA, USA, 20–22 June, DFNE 18–781.
- Farkas, M.P., Hofmann, H., Yoon, J.S., Zimmermann, G., Zang, A. & Stephansson, O., 2017. Numerical investigation of hydraulic stimulation and related induced seismicity in Pohang fractured geothermal reservoir, in *Proceedings of the 12th EURO-conference on Rock Physics and Geomechanics*, Ma’ale HaHamisha, Israel, 5–10 November.
- Fokker, P.A., Hofmann, H., Meier, P., Min, K.-B., Yoon, K. & Zimmermann, G., 2018a. Harmonic pulse testing as a monitoring tool during hydraulic stimulation of an enhanced geothermal system, in *Proceedings of the 43rd Workshop on Geothermal Reservoir Engineering*, Stanford, CA, USA, 12–14 February, SGP-TR-213.
- Fokker, P.A., Salina Borello, E., Verga, F. & Viberti, D., 2018b. Harmonic pulse testing for well performance monitoring, *J. Petrol. Sci. Eng.*, **162**, 446–459.
- Font, Y., Kao, H., Lallemand, S., Liu, C.-S. & Chiao, L.-Y., 2004. Hypocentre determination offshore of eastern Taiwan using the Maximum Intersection method, *Geophys. J. Int.*, **158**(2), 655–675.
- García-García, J.M., Vidal, F., Romacho, M.D., Martín-Marfil, J.M., Posadas, A. & Luzin, F., 1996. Seismic source parameters for microearthquakes of the Granada basin (southern Spain), *Tectonophysics*, **261**(1–3), 51–66.
- Garg, S.K. & Combs, J., 1997. Use of slim holes with liquid feed zones for geothermal reservoir assessment, *Geothermics*, **26**(2), 153–178.
- Gaucher, E., Schoenball, M., Heidbach, O., Zang, A., Fokker, P.A., van Wees, J.D. & Kohl, T., 2015. Induced seismicity in geothermal reservoirs: a review of forecasting approaches, *Renew. Sust. Energ. Rev.*, **52**, 1473–1490.
- Giardini, D., 2009. Geothermal quake risks must be faced, *Nature*, **462**, 848–849.
- Grant, M.A., Clearwater, J., Quinao, J., Bixley, P.F. & Le Brun, M., 2013. Thermal stimulation of geothermal wells: a review of field data, in *Proceedings of the 38th Workshop on Geothermal Reservoir Engineering*, Stanford, CA, USA, 11–13 February, SGP-TR-198.
- Grigoli, F. *et al.*, 2018. The November 2017 Mw 5.5 Pohang earthquake: a possible case of induced seismicity in South Korea, *Science*, **360**(6392), 1003–1006.
- Hanks, T.C. & Kanamori, H., 1979. A moment magnitude scale, *J. geophys. Res.*, **84**(B5), 2348–2350.
- Hastings, W.K., 1970. Monte Carlo sampling methods using Markov chains and their applications, *Biometrika*, **57**(1), 97–109.
- Hofmann, H., Zimmermann, G., Zang, A. & Min, K.-B., 2018b. Cyclic soft stimulation (CSS): a new fluid injection protocol and traffic light system to mitigate seismic risks of hydraulic stimulation treatments, *Geotherm. Ener.*, **6**(1), 27, doi:10.1186/s40517-018-0114-3.
- Hofmann, H. *et al.*, 2017. First field application of a cyclic injection protocol and an advanced traffic light system to mitigate the seismic risk from hydraulic stimulation at the Pohang Enhanced Geothermal System project site in Korea, in *Proceedings of the 12th EURO-Conference on Rock Physics and Geomechanics*, Ma’ale HaHamisha, Israel, 5–10 November.
- Hofmann, H. *et al.*, 2018a. Comparison of cyclic and constant fluid injection in granitic rock at different scales, in *Proceedings of the 52nd US Rock Mechanics / Geomechanics Symposium*, Seattle, WA, USA, 17–20 June, ARMA 18–691.
- Horne, R.N., 1995. *Modern well test analysis: a computer-aided approach*, 2nd edition, Petroway Inc, Palo Alto.
- Huenges, E., Trautwein, U., Legarth, B. & Zimmermann, G., 2006. Fluid pressure variation in a sedimentary geothermal reservoir in the North German Basin: case study Groß Schönebeck, *Pure Appl. Geophys.*, **163**, 2141–2152.
- Huenges, E., Zang, A. & Kim, K.Y., 2017. Soft stimulation and induced seismicity, in *Proceedings of the Schatzalp Workshop on Induced Seismicity*, Davos, Switzerland, 14–17 March.

- Jolivet, L. & Tamaki, K., 1992. Neogene kinematics in the Japan Sea region and volcanic activity of the northeast Japan Arc, *Proc. Ocean Drilling Prog., Scient. Results*, **127/128(2)**, 1311–1331.
- Jurkevics, A., 1988. Polarization analysis of three-component array data, *Bull. seism. Soc. Am.*, **78(5)**, 1725–1743.
- Kaven, J.O., Hickman, S.H. & Davatzes, N.C., 2014. Micro-seismicity and seismic moment release within the Coso Geothermal Field, California, in *Proceedings of the 39th Workshop on Geothermal Reservoir Engineering*, Stanford, CA, USA, 24–26 February, SGP-TR-202.
- Kaya, E., Zarrouk, S.J. & O'Sullivan, J., 2011. Reinjection in geothermal fields: a review of worldwide experience, *Renew. Sust. Energ. Rev.*, **15(1)**, 47–68.
- Kim, H., Xie, L., Min, K.-B., Bae, S. & Stephansson, O., 2017b. Integrated in situ stress estimation by hydraulic fracturing, borehole observations and numerical analysis at the EXP-1 borehole in Pohang, Korea, *Rock Mech. Rock Eng.*, **50(12)**, 3141–3155.
- Kim, H.C. & Lee, Y., 2007. Heat flow in the Republic of Korea, *J. geophys. Res.*, **112**, B05413, doi:10.1029/2006JB004266.
- Kim, K.-H., Ree, J.-H., Kim, Y.H., Kim, S., Kang, S.Y. & Seo, W., 2018a. Assessing whether the 2017 Mw 5.4 Pohang earthquake in South Korea was an induced event, *Science*, **360(6392)**, 1007–1009.
- Kim, K.-I. et al., 2018b. Protocol for induced microseismicity in the first enhanced geothermal systems project in Pohang, Korea, *Renew. Sust. Energ. Rev.*, **91**, 1182–1191.
- Kim, M., Yoon, B., Lee, C., Park, K.G., Yoon, W.-S., Song, Y. & Lee, T.J., 2017a. Microseismic monitoring during hydraulic stimulation in Pohang (Korea) for EGS pilot project, in *Proceedings of the American Geophysical Union Fall Meeting*, New Orleans, LA, USA, 11–15 December.
- Kim, Y.H., Rhie, J., Kang, T.-S., Kim, K.-H., Kim, M. & Lee, S.-J., 2016. The 12 September 2016 Gyeongju earthquakes: 1. Observation and remaining questions, *Geosci. J.*, **20(6)**, 747–752.
- KMA - Korea Meteorological Administration, 2018. <http://www.weather.go.kr/weather/earthquake.volcano/report.jsp>, accessed on 09.07.2018.
- Kwiatek, G. & Ben-Zion, Y., 2016. Theoretical limits on detection and analysis of small earthquakes, *J. geophys. Res.*, **121(8)**, 5898–5916.
- Kwiatek, G., Bohnhoff, M., Dresen, G., Schulze, A., Schulte, T., Zimmermann, G. & Huenges, E., 2010. Microseismicity induced during Fluid-Injection: A case study from the geothermal site at Groß Schönebeck, North German Basin, *Acta Geophys.*, **58(6)**, 995–1020.
- Kwon, S. et al., 2018. Characterization of 4.2-km-deep fractured granodiorite cores from Pohang Geothermal Reservoir, Korea, *Rock Mech. Rock Eng.*, doi:10.1007/s00603-018-1639-2.
- Lagarias, J.C., Reeds, J.A., Wright, M.H. & Wright, P.E., 1998. Convergence properties of the Nelder–Mead simplex method in low dimensions, *SIAM J. Optim.*, **9(1)**, 112–147.
- Lee, J., 1982. *Well Testing*, SPE Textbook Series, vol. 1, pp. 159, Society of Petroleum Engineers.
- Lee, R., Chang, C., Hong, T.-K., Lee, J., Bae, S.-H., Park, E.-S. & Park, C., 2016. A comparison between deep and shallow stress fields in Korea using earthquake focal mechanism inversions and hydraulic fracturing stress measurements, *Geophys. Res. Abst.*, **18**, EGU2016–11721–3.
- Lee, T.-H., Yi, K., Cheong, C.-S., Jeong, Y.-J., Kim, N. & Kim, M.-J., 2014. SHRIMP U-Pb zircon geochronology and geochemistry of drill cores from the Pohang Basin, *J. Petrol. Soc. Korea*, **23(3)**, 167–185.
- Lee, T.J., Song, Y., Park, D.-W., Jeon, J. & Yoon, W.S., 2015. Three dimensional geological model of Pohang EGS Pilot Site, Korea, in *Proceedings of the World Geothermal Congress*, Melbourne, Australia, 19–25 April, Paper No. 31025.
- Lee, T.J., Song, Y., Yoon, W.S., Kim, K.Y., Jeon, J., Min, K.-B. & Cho, Y.-H., 2011. The first enhanced geothermal system project in Korea, in *Proceedings of the 9th Asian Geothermal Symposium*, pp. 129–132, Kahoshima, Japan, 7–9 November.
- Lee, Y., Park, S., Kim, J., Kim, H.C. & Koo, M.H., 2010. Geothermal resource assessment in Korea, *Renew. Sust. Energ. Rev.*, **14(8)**, 2392–2400.
- Lomax, A., 2005. A reanalysis of the hypocentral location and related observations for the great 1906 California Earthquake, *Bull. seism. Soc. Am.*, **95(3)**, 861–877.
- Majer, E., Baria, R., Stark, M., Oates, S., Bommer, J., Smith, B. & Asanuma, H., 2007. Induced seismicity associated with enhanced geothermal systems, *Geothermics*, **36(3)**, 185–222.
- Majer, E., Nelson, J., Robertson-Tait, A., Savy, J. & Wong, I., 2012. Protocol for addressing induced seismicity associated with Enhanced Geothermal Systems, DOE-EE-0662, Downloaded on 11.01.2018 from: https://www1.eere.energy.gov/geothermal/pdfs/geothermal_seismicity_protocol_012012.pdf.
- McClure, M.W. & Horne, R.N., 2014. An investigation of stimulation mechanisms in enhanced geothermal systems, *Int. J. Rock Mech. Min.*, **72**, 242–260.
- Meier, P.M., Rodriguez, A.A. & Bethmann, F., 2015. Lessons learned from Basel: new EGS projects in Switzerland using multistage stimulation and a probabilistic traffic light system for the reduction of seismic risk, in *Proceedings of the World Geothermal Congress*, Melbourne, Australia, 19–25 April, Paper No. 31023.
- Messer, P.H., Pye, D.S. & Gallus, J.P., 1978. Injectivity restoration of a hot-brine geothermal injection well, *J. Petrol. Technol.*, **30(9)**, 1225–1230.
- Metropolis, N., Rosenbluth, A., Rosenbluth, M., Teller, A. & Teller, E., 1953. Equation of state calculations by fast computing machines, *J. Chem. Phys.*, **21**, 1087–1092.
- Michelet, S. & Toksöz, M.N., 2007. Fracture mapping in the Soultz-sous-Forêts geothermal field using microearthquake locations, *J. geophys. Res.*, **112(B7)**, B07315, doi:10.1029/2006JB004442.
- Mo, L. & Harris, J.M., 1995. Analysis and attenuation of tube waves in crosswell seismic survey, *SEG Technical Program Expanded Abstracts*, 438–441, doi:10.1190/1.1887359.
- Nelder, J. & Mead, R., 1965. A simplex method for function minimization, *Comput. J.*, **7(4)**, 308–313.
- Park, S., Xie, L., Kim, K.-I., Kwon, S., Min, K.-B., Choi, J., Yoon, W.-S. & Song, Y., 2017a. First hydraulic stimulation in fractured geothermal reservoir in Pohang PX-2 well, *Proc. Eng.*, **191**, 829–837.
- Park, S. et al., 2017b. Hydraulic stimulation in fractured geothermal reservoir in Pohang PX-1 well, in *Proceedings of the Ysrm 2017 & Ndrmg 2017*, pp. 373–374, Jeju, Korea, May 10–13.
- Park, Y., Ree, J.-H. & Yoo, S.-H., 2006. Fault slip analysis of Quaternary faults in southeastern Korea, *Gondwana Res.*, **9(1-2)**, 118–125.
- Pasikki, R.G., Libert, F., Yoshioka, K. & Leonard, R., 2010. Well stimulation techniques applied at the Salak geothermal field, in *Proceedings of the World Geothermal Congress*, Bali, Indonesia, 25–30 April, Paper No. 2274.
- Patel, S.M., Sondergeld, C.H. & Rai, C.S., 2017. Laboratory studies of hydraulic fracturing by cyclic injection, *Int. J. Rock Mech. Min.*, **95**, 8–15.
- Schulte, T., Zimmermann, G., Vuataz, F., Portier, S., Tischner, T., Junker, R., Jatho, R. & Huenges, E., 2010. Enhancing Geothermal Reservoirs, in *Geothermal Energy Systems: Exploration, Development, and Utilization*, eds Huenges, E. & Ledru, P., Wiley, doi:10.1002/9783527630479.ch4.
- Snoke, J. A., 1987. Stable determination of (Brune) stress drop, *Bull. seism. Soc. Am.*, **77(2)**, 530–538.
- Song, Y., Lee, T.J., Jeon, J. & Yoon, W.S., 2015. Background and progress of the Korean EGS pilot project, in *Proceedings of the World Geothermal Congress*, Melbourne, Australia, 19–25 April, Paper No. 01008.
- Son, M., Song, C.W., Kim, M.-C., Cheon, Y., Cho, H. & Sohn, Y.K., 2015. Miocene tectonic evolution of the basins and fault systems, SE Korea: dextral, simple shear during the East Sea (Sea of Japan) opening, *J. Geol. Soc. Lond.*, **172**, 664–680.
- Stefánsson, V., 1997. Geothermal reinjection experience, *Geothermics*, **26(1)**, 99–139.
- Stephansson, O., Semikova, H., Zimmermann, G. & Zang, A., 2018. Laboratory pulse test of hydraulic fracturing on granitic sample cores from Äspö HRL, Sweden, *Rock Mech. Rock Eng.*, doi:10.1007/s00603-018-1421-5.
- Wiemer, S., Kraft, T., Trutnevyte, E. & Roth, P., 2017. “Good Practice” Guide for Managing Induced Seismicity in Deep Geothermal Energy Projects in Switzerland, Version 1.0, Swiss Seismological Service (SED), October 2017, Downloaded on 11.01.2018 from: http://seismo.ethz.ch/export/sites/sedsite/research-and-teaching/galleries/pdf_products.softw

- are/Good-Practice-Guide-for-Managing-Induced-Seismicity-in-Deep-Geothermal-Energy-Projects-in-Switzerland.v1.0.pdf.
- Wu, C. & Harris, J.M., 2004. Cross-well seismic modeling with inclusion of tube waves and tube-wave-related arrivals, *Geophys. Res. Lett.*, **31**, L11606, doi:10.1029/2004GL019873.
- Yoon, J.S., Zimmermann, G. & Zang, A., 2015a. Discrete element modeling of cyclic rate fluid injection at multiple locations in naturally fractures reservoirs, *Int. J. Rock Mech. Min.*, **74**, 15–23.
- Yoon, K.-S., Jeon, J.-S., Hong, H.-K., Kim, H.-G., Hakan, A., Park, J.-H. & Yoon, W.S., 2015b. Deep drilling experience for Pohang enhanced geothermal project in Korea, in *Proceedings of the World Geothermal Congress*, Melbourne, Australia, 19–25 April, Paper No. 06034.
- Zang, A., Oye, V., Jousset, P., Deichmann, N., Gritto, R., McGarr, A., Majer, E. & Bruhn, D., 2014. Analysis of induced seismicity in geothermal reservoirs – an overview, *Geothermics*, **52**, 6–21.
- Zang, A., Stephansson, O. & Zimmermann, G., 2017b. Keynote: fatigue hydraulic fracturing, *Proc. Eng.*, **191**, 1126–1134.
- Zang, A., Yoon, J.S., Stephansson, O. & Heidbach, O., 2013. Fatigue hydraulic fracturing by cyclic reservoir treatment enhances permeability and reduces induced seismicity, *Geophys. J. Int.*, **195**(2), 1282–1287.
- Zang, A., Zimmermann, G., Hofmann, H., Stephansson, O., Min, K.-B. & Kim, K.Y., 2018. How to reduce fluid-injection-induced seismicity, *Rock Mech. Rock Eng.*, doi:10.1007/s00603-018-1467-4.
- Zang, A. *et al.*, 2017a. Hydraulic fracture monitoring in hard rock at 410 m depth with an advanced fluid-injection protocol and extensive sensor array, *Geophys. J. Int.*, **208**(2), 790–813.
- Zhou, H., 1994. Rapid three-dimensional hypocentral determination using a master station method, *J. geophys. Res.*, **99**(B8), 15 439–15 455.
- Zhuang, L. *et al.*, 2016. Laboratory study on cyclic hydraulic fracturing of Pocheon granite in Korea, in *Proceedings of the 50th US Rock Mechanics / Geomechanics Symposium*, Houston, TX, USA, 26–29 June, ARMA 16–163.
- Zhuang, L. *et al.*, 2017. Laboratory evaluation of induced seismicity reduction and permeability enhancement effects of cyclic hydraulic fracturing, in *Proceedings of the 51st US Rock Mechanics / Geomechanics Symposium*, San Francisco, CA, USA, 25–28 June, ARMA 17–757.
- Zhuang, L. *et al.*, 2018. Cyclic hydraulic fracturing of cubic granite samples under triaxial stress state with acoustic emission, injectivity and fracture measurements, in *Proceedings of the 52nd US Rock mechanics / Geomechanics Symposium*, Seattle, WA, USA, 17–20 June, ARMA 18–297.
- Zimmermann, G., Moeck, I. & Blöcher, G., 2010. Cyclic waterfrac stimulation to develop an Enhanced Geothermal System (EGS) – conceptual design and experimental results, *Geothermics*, **39**(1), 59–69.
- Zimmermann, G. *et al.*, 2015. Multi-fracturing and cyclic hydraulic stimulation scenarios to develop enhanced geothermal systems – feasibility and mitigation strategies to reduce seismic risk, in *Proceedings of the World Geothermal Congress*, Melbourne, Australia, 19–25 April, Paper No. 31009.

SUPPORTING INFORMATION

Supplementary data are available at [GJI](#) online.

Please note: Oxford University Press are not responsible for the content or functionality of any supporting materials supplied by the authors. Any queries (other than missing material) should be directed to the corresponding author for the paper.